Abradable Sealing Materials for Emerging IGCC-Based Turbine Systems

FINAL SCIENTIFIC/TECHNICAL REPORT

Reporting Period Start Date: October 1st, 2013
Reporting Period End Date: August 14th, 2017

Principal Author

Prof. Daniel R. Mumm
Tel: (949) 824-3858; Email: mumm@uci.edu

Report Issued: March 27th, 2019

WORK PERFORMED UNDER AGREEMENT: DE-FE0011929

SUBMITTED BY
The Regents of the University of California, Irvine
5171 California, Avenue, Suite 150
University of California, Irvine
Irvine, CA 92697
DUNS: 04-670-5849

SUBMITTED TO
Robin Ames (Project Manager)
U. S. Department of Energy
National Energy Technology Laboratory
Morgantown, WV 26507-0880
Tel: (304) 285-0978; Email: robin.ames@netl.doe.gov

ABSTRACT

Reducing the gap between rotating and stationary parts in gas turbine engines, and mitigating gas leakage via these paths, can significantly increase the performance and attendant efficiency. One approach to reducing such gaps is to deploy abradable coatings on the stationary shroud components as seals, to reduce the blade-tip clearances under operational conditions. Abradable coatings must be able to withstand high temperature oxidation, thermal cycling, and erosion, while providing optimal controlled abrasion and associated shape retention. Existing abradable seals utilized in power generation turbines have generally been optimized for use with natural gas-fired systems; however, preliminary testing of syngas and high-hydrogen-content (HHC) fired turbines has shown that the stability of hot-section materials (and presumably abradable sealing materials) may be substantially altered due to characteristic changes in the combustion by-products (partial pressures of water vapor, etc.) as well as characteristic impurities and particulate matter entrained in the fuel. The primary focus of this research program has been to develop a mechanistic understanding of how the altered combustion environments modify the thermo-mechanical stability and performance of the sealing materials, including the requisite abradable sealing behavior. A key component of the research program carried out has been an exploration of *mechanisms* underpinning observed degradation processes, and an assessment of connections to the combustion environments and characteristic non-combustible constituents. The ultimate goal of the project has been to advance the goals of the *Advanced Turbine Program* by developing materials design protocols leading to turbine hot-section components with improved resistance to service lifetime degradation under advanced fuels exposures.

This research program has evaluated the performance and degradation of ceramic abradable seals used in the high-temperature turbine sections of gas turbine engines. The focus has been two-fold: (1) to understand performance of such materials in relation to the turbines operating on coal-derived syngas and high hydrogen content (HHC) fuels, ultimately seeking an improved understanding of factors that control performance and durability of abradable seal materials for these combustion environments (and play into materials design protocols); and (2) to evaluate the potential of alternative materials as abradable seals for the higher temperatures expected with IGCC and HHC fueled turbine systems. In particular, we carried out an initial assessment of multi-layered systems of existing abradable seal materials (YSZ) and other ceramics.

The research program also investigated several classes of abradable coatings under simulated exposures to syngas-based combustion environments, evaluating the relevant wear behavior, hardness, stability under cyclic oxidation, and general thermo-mechanical behavior. The research also attempted to develop alternatives to carrying out full-scale combustion-based abradability test rig exposures to evaluate materials system performance. The research has been focused on correlating the measured thermo-mechanical behavior, and controlled abrasive wear, with the intrinsic properties of the multilayer coatings and processing-controlled microstructural features that have shown attractive machinability characteristics based on weak interfacial bonding between the constituent phases at elevate temperatures (while maintaining thermochemical stability).

This program has resulted in an improved mechanistic understanding of factors governing performance of high temperature abradable seals, and degradation mechanisms unique to IGCC-based power generation turbine systems and the realization of coal-derived syngas and HHC-based combustion environments – ultimately with the goal of developing a knowledge base upon which the design of coatings that retain optimal sealing characteristics and are more resistant to the observed wear/attack mechanisms, important aspects of advancing the goals of the DOE Advanced Turbine Program.

TABLE OF CONTENTS

EXECUTIVE SUMMARY

Reducing the gap between rotating and stationary parts in gas turbine engines, and mitigating gas leakage via these paths, can significantly increase the performance and attendant efficiency. One approach to reducing such gaps is to deploy abradable coatings on the stationary shroud components as seals, to reduce the blade-tip clearances under operational conditions. Abradable coatings must be able to withstand high temperature oxidation, thermal cycling, and erosion, while providing optimal controlled abrasion and associated shape retention. Existing abradable seals utilized in power generation turbines have generally been optimized for use with natural gas-fired systems; however, preliminary testing of syngas and high-hydrogen-content (HHC) fired turbines previously suggested that the stability of hot-section materials (and presumably abradable sealing materials) may be substantially altered due to characteristic changes in the combustion by-products (partial pressures of water vapor, etc.) as well as characteristic impurities and particulate matter entrained in the fuel. As such, the overarching goal of this research program has been to evaluate the potential impacts of coal-derived syngas and high-hydrogen content fuels on the degradation of abradable seals, while developing a mechanistic understanding of how the altered combustion environments modify the thermo-mechanical performance of the sealing materials – including the requisite abradable sealing behavior. Based on establishing a more complete, mechanistic understanding of how these emerging fuel streams affect materials degradation, the ultimate goal of the program has been to advance the goals of the *Advanced Turbine Program* by developing materials design protocols for turbine hot-section abradable coatings with improved resistance to service lifetime degradation under advanced fuels exposures.

The overall research program has been directed at characterizing the performance and degradation of abradable seals used in the high-temperature turbine sections of gas turbine engines. The focus has been two-fold: (1) to understand performance of such materials in relation to the turbines operating on coal-derived syngas and high hydrogen content (HHC) fuels, ultimately seeking an improved understanding of factors that control performance and durability of abradable seal materials for these combustion environments (and play into materials design protocols); and (2) to evaluate the potential of alternative materials as abradable seals for the higher temperatures expected with IGCC and HHC fueled turbine systems. Specifically, the objectives of this project have been to investigate the impacts of coal-derived syngas combustion environments on the performance, durability and degradation of *existing* abradable coatings used on turbine shroud structures, while assessing the potential of *alternative* materials sets for improving performance of hot-section abradable seals in integrated gasification combined cycle (IGCC) based gas turbine power plants. The program investigated several classes of abradable coatings (including currently utilized metal and ceramic-based systems) under simulated exposures to syngas-based combustion environments – evaluating the relevant wear/abrasive recession behavior, hardness, stability under cyclic oxidation, and general thermo-mechanical behavior. In the latter stages of the program, we have evaluated composites of existing abradable seal materials (YSZ) and rare earth phosphates that have shown attractive machinability characteristics based on weak interfacial bonding between the constituent phases at elevate temperatures (while maintaining thermochemical stability). Overall, the research has been focused on correlating the measured thermo-mechanical behavior, and controlled abrasive wear, with the intrinsic properties of the multilayer coatings, processing-controlled microstructural features, and service environment exposures.

The research was also aimed at the development of a combustion-based abradability test rig, leveraging previous UCI activities and infrastructure for burner rig testing and combustion-based materials exposure experiments. The research has been focused on correlating the measured thermo-mechanical behavior, and controlled abrasive wear, with the intrinsic properties of the multilayer coatings and processing-controlled microstructural features, and developing a comprehensive mechanistic understanding of factors governing performance of high temperature abradable seals, and degradation mechanisms unique to IGCC-based

power generation turbine systems and the realization of coal-derived syngas and HHC-based combustion environments. The resulting knowledge base is expected to assist in the design of coatings that retain optimal sealing characteristics in systems fueled with the emerging alternative fuel streams, however are more resistant to the observed wear/attack mechanisms – important aspects of advancing the goals of the *DOE Advanced Turbine Program*. The scope of the program spans six themes which are inter-related towards achieving the overarching goal of attaining more stable, durable abradable seal systems for use in coal-derived syngas and high hydrogen content (HHC) environments. These themes include: (1) performance examination of existing high temperature abradable seal coatings, and identification of materials evolution and degradation mechanisms specific to syngas and HHC combustion environments; (2) oxidation behavior of abradable seal materials (in particular, those based on air plasma spray (APS) MCrAlY coatings) unique to HHC environmental exposures; (3) high-resolution imaging and microanalysis to explore abrasive recession and seal definition variations as a function of combustion environments (e.g., are the oxidative processes, sintering or phase destabilization of the seal materials accelerated in high water vapor environments such that seal performance is degraded); (4) thermo-mechanical drivers and thermal gradient effects on the needed abrasive wear processes, as well as seal failure through cracking and delamination (including testing under thermal gradient exposures); (5) potential impacts of melting of particulate matter entrained in the gas flow stream, and infiltration into the seal coatings, and reaction products and evolving phases associated with molten phase corrosion mechanisms; and (6) alternative materials (including new compositions or bi-layer concepts) with potential for use as high temperature seals with improved performance in emerging aggressive combustion environments.

As a core component of this program, we have explored possible routes for acceleration of the degradation of sealing materials in syngas and high hydrogen content fueled turbine systems related to the sintering and microstructural evolution of porous ceramic abradable coatings. Primary outcomes of the program include (1) evaluating key microstructural features that enhance the performance of ceramic abradable coatings; and (2) *demonstrating that elevated water vapor content in the combustion gas stream (typical of IGCC systems and those utilizing HHC fuels) plays a crucial role in the kinetics of attack and coating degradation – generally accelerating the phase evolution and aging degradation of the desirable phase composition of YSZ-based abradable coatings.* The action of high water vapor content environments in accelerating the aging of abradable coatings through the evolution of the t' phase to the equilibrium cubic and monoclinic phases has been assessed through isothermal testing in controlled environments, measurement of phase evolution by Raman and X-ray spectroscopy, and assessment of the time-dependent phase constitution. *Although additional verification is needed, the results generated in this program suggest an important role of fuel type on the kinetics of abradable coating degradation.*

REPORT DETAILS

1. General Background

Gas turbine engines are currently used in the production of approximately 30% of the electricity generated in the U.S. – a number that is expected to rise as the shale gas market matures – which dictates that the country's energy costs and policies will be significantly influenced by turbine efficiency and fuel. Integrated Gasification Combined Cycle (IGCC) power plants promise to improve both, as they transform coal, biomass and other carbon feedstocks into clean, synthetic gas (syngas) that can either be reprocessed into liquid fuel for use in aero turbines, or converted into electricity at the plant – via gas turbine – with ~45% efficiency and full carbon capture. From a materials standpoint, it is critical to understand how combusting syngas at IGCC turbine inlet temperatures (e.g. 1425^{0}C and rising) may affect degradation mechanisms of abradable coating system constituents, for systems that are used to protect hot section components [1]. In particular, it is important to understand how the degradation mechanisms might differ from ones associated with combusting natural gas, the conventional gas turbine fuel for which materials were originally optimized. Higher water vapor levels in the combustion zone are one expected consequence of using high-hydrogen content fuels such as syngas. A study done by the National Energy Technology Laboratory (U.S. Department of Energy) [2] indicates that water vapor is expected to account for 12-14% of the turbine exhaust; industry use of steam injection to suppress NO_x may raise the total to 25-30%, representing as much as a four-fold increase over that derived from natural gas combustion. Therefore, it is important to understand the role of high water vapor content in the material degradation of YSZ-based coating systems in the combustion environment of gas turbines.

2. Accelerated Aging of the Yttria-Stabilized Zirconia Matrix of Baseline Ceramic Abradable Coatings

Background and Approach – The degradation of the ceramic matrix used in common abradable coatings – 8wt% yttria stabilized zirconia (8YSZ) – has received increased attention recently as IGCC turbine inlet temperatures continue to rise, e.g. 1425 °C or higher [2]. One major degradation mechanism is the tetragonal phase of 8YSZ – referred to as *t'* – decomposing to its equilibrium mixture of yttrium-rich cubic phase and yttrium-lean tetragonal phase given a sufficient thermodynamic driving force, as shown schematically in **Figure 1**. The metastable *t'* phase has been shown to transform to these more stable phases – as well as the continued transformation of the tetragonal phase to the monoclinic phase below the martensitic temperature – upon aging in laboratory-air environments at temperatures in excess of 982ºC [3-6]. The resulting stable phases form a coherent array of Y-rich (cubic + *t''*) and Y-lean (t + m) phases at the expense of the *t'* phase. In a recent study by Krogstad, *et al.*,[7] the inferred gradient in the degree of tetragonality across these coherent interfaces was used as evidence for a spinodal decomposition as opposed to a nucleation-and-growth mechanism. This destabilization of the *t'* phase has been found to occur in 8YSZ for both electron beam physical vapor deposition (EBPVD) coatings used in aero-propulsion turbines and APS coatings predominately used in power generation systems [3,4]. While both EBPVD and APS coatings have been shown to follow the same trend in destabilization of the *t'*-phase with aging, a direct comparison of these two coatings showed distinct differences in the phase evolution of the stable Y-rich and Y-lean phases after the initial destabilization of the *t'* phase [3].

While previous studies of the destabilization of the *t'* phase at elevated temperatures have generally focused on dry or laboratory-air environments, the low-temperature degradation (LTD) of YSZ has focused on the destabilization of the tetragonal phase in humid environments. In LTD, the tetragonal phase of the YSZ transforms to the monoclinic phase at temperatures less than 300ºC in moist air. LTD in humid environments was first identified by Kobayashi *et al.*[8] who reported on the presence of micro-cracking and the loss in strength after the tetragonal to monoclinic transformation in YSZ. Since this early finding, additional papers have identified some general characteristics of LTD which include: (a) the phase

transformation originating from the surface, and (b) resistance to the phase transformation increasing with higher stabilizer content or smaller grain sizes [9-11]. Many mechanisms have been proposed for trying to understand the monoclinic to tetragonal phase transformation that occurs during LTD in humid environments. Yoshimura *et al.* [12] proposed that water cleaves Zr-O-Zr bonds at the surface of t-YSZ causing the formation of Zr-OH or Y-OH. The formation of these hydroxyl groups was said to cause a stress field that induced the monoclinic phase transformation. Along the same lines, Sato and Shimada [10] proposed that the chemisorption of water on the surface of t-YSZ formed Zr-OH, which in turn caused the surface energy difference to be reduced between the tetragonal and monoclinic grains. However, this model is limited in that it does not explain the dependence of the tetragonal-to-monoclinic transformation on the grain size and stabilizer content [13].

In a different proposed LTD model, Lange *et al.*[11] suggested that α-$Y(OH)_3$ formation created yttria-poor regions at the surface, which then serve as nucleation sites for the monoclinic phase. This explanation was largely debunked by Kim *et al.*, [13] where 3 mol% YSZ samples were aged by LTD, annealed for two hours, and then aged by LTD again. The authors found that the YSZ transformed to the monoclinic phase after the initial aging, reversed to the tetragonal phase by the annealing treatment, and then transformed back to the monoclinic phase again after aging – but with significantly less transformation than after the first aging treatment. If Y_2O_3 was being depleted from the sample by hydroxide formation during the initial aging treatment, then subsequent aging should have caused further LTD due to less stabilizer content – but this did not occur. These authors also doped t-YSZ with Nb_2O_5 and showed the activation enthalpy for LTD was constant regardless of the dopant amount and grain size. The authors suggested that LTD was a cause of thermally-activated oxygen vacancy diffusion where the pentavalent dopant annihilated oxygen vacancies and thus decreased the oxygen diffusion rate – and therefore the rate of LTD. This explanation is consistent with the annealing anion vacancy model of LTD [14,15]. According to this model, water dissociates at the surface of t-YSZ to produce interstitial hydrogen ions and oxygen anions which anneal anion vacancies. Although this annealing anion vacancy model is appealing, it has not yet been proven that oxygen anions or some other water derived species is entering the 8YSZ and altering the thermodyamics and/or kinetics of the tetragonal phase transformation.

Even if oxygen anions are entering 8YSZ, this still leaves protons unaccounted for in their role in influencing the phase evolution of the *t'* phase. As protons derived from water would be more numerous, more mobile, and can occupy more locations in the lattice than the oxygen anions, they would seem to have a much more influential role than oxygen anions in destabilization pathways. While protons are not considered the dominant ion conductor in YSZ, computational studies have shown that the energy associated with proton migration in YSZ is comparable to other proton conductors like $BaZrO_3$ [16,17]. At temperatures relevant to LTD, protons were found to diffuse into single crystal tetragonal YSZ as determined by a SIMS analysis [18]. A different study measured the electrical conductivity of 3 mol% YSZ thin films in dry and humid environments across a range of temperatures [19]. The porous films showed a dramatic increase in overall conductivity in the temperature rang of 120 to 400 °C for the humid environment which the authors attributed to proton conduction. While it was only speculated that this was due to the formation of hydroxyl groups at the surface of YSZ, a separate study verified the presence of hydroxyl groups in YSZ thin films by exposing them to a deuterium oxide (D_2O) gas environment [20]. XPS on the exposed samples confirmed that hydroxyl ions were present on the sample even after etching the sample with Ar in the XPS chamber. The study also confirmed proton migration by measuring an open circuit voltage in a hydrogen/air fuel cell that disallowed oxygen migration due to the presence of a palladium interlayer. Therefore, there is evidence for protons to be incorporated into YSZ and migrate through the material in humid environments.

Both LTD in humid environments and high temperature aging in dry environments of 8YSZ have been shown to de-stabilize the *t'* or tetragonal phase to the monoclinic and other stable phases. However, what has not been shown is whether the de-stabilization of the *t'* phase is accelerated at high temperatures –

relevant to gas turbines – for long exposures in high water vapor content environments. This study demonstrates that aging 8YSZ in a high-temperature, humid environment does indeed accelerate the de-stabilization of the *t'* phase in comparison to that of a dry environment exposure. Furthermore, the mechanism of proton incorporation by hydroxyl group formation will be invoked to explain how water vapor species emanating from exposure to high water vapor content environments enhances the destabilization of the *t'* phase. Clarifying the role of water vapor in the high temperature degradation of 8YSZ will allow for more detailed investigations into the role of water species in the phase evolution of the *t'* phase at temperatures relevant to gas turbine power generation.

Experimental Methods – A free-standing plate of APS 8YSZ, with a thickness of ~ 3mm, was fabricated at the Forschungszentrum Jülich research center in Jülich, Germany. The coating was applied with a Triplex II torch from Oerlikon Metco, Wohlen, Switzerland. A commercially available powder Metco 204NS also by Oerlikon Metco was used. The gun current was adjusted to 510A and provided with process gases of 50 slpm Ar and 4slpm He, providing a power of 57 kW. The stand-off distance was 200 mm. The resulting material had approximately ~17% porosity, representative of commercial applications of APS YSZ in power generation combustion systems. The APS 8YSZ was sectioned with a slow-speed diamond blade saw prior to aging experiments.

Isothermal aging was carried out at 1330º C in an environmentally controlled furnace. For all aging experiments, samples were placed on top of loose 3 mol% YSZ powder to prevent diffusion between the samples and the crucible. All aging experiments were conducted at a fixed ramp-rate of 4°C/min, and the aging times varied between 6-570 h as determined by approximate LMP intervals. As the temperature was fixed at 1330º C for all aging experiments, a change in the LMP corresponds to a change in the aging time. Each sample was aged for only one aging time and not re-used for additional aging (e.g. the 140 h aged sample was not reused to achieve an aging time of 224 h as illustrated in **Figure 2**). The exposure environment consisted of a gas mixture of ultra-high purity N_2 and O_2 that was flowed through the furnace tube at a rate of 80 mL/min. The flow rates for both gases were chosen so that the partial pressure of oxygen was fixed at 0.2 atm for both the dry and humid environments. Prior to ramping the furnace to the aging temperature of either the dry or humid environment, the tube furnace was purged of laboratory air for six residence times of gas flow. For the humid-aging environment, a second purge was carried out to replace the dry environment with the humid one for another six residence times of gas flow while the furnace was held at 150ºC. All humid-aging tests were performed at a water vapor content of 45 vol% by bubbling the N_2/O_2 gas mixture through a water bath at a controlled bath temperature. After each humid-aging test, the condensed water vapor from the tube furnace exhaust was weighed to ensure that the controlled environment had a water vapor content of 45 vol%.

Post-aging phase identification in the aged samples was achieved by XRD and Raman spectroscopy to determine if the *t'* phase of the 8YSZ was destabilized faster in a humid environment. XRD was performed using a step size of 0.004 deg with a scan speed of 1 deg/min on a 1D silicon-strip detector. In order to achieve a more-localized phase identification than XRD, Raman spectroscopy was performed. Prior to collecting spectra from aged samples, the instrument was calibrated using the 520.5 cm^{-1} Raman band of a silicon wafer. Spectra were excited using a laser operating at a wavelength of 532 nm.

A Rietveld refinement analysis was performed on the XRD spectra using the *General Structure Analysis System* (GSAS) software with the EXPGUI graphical user interface [21] in order to quantify the phase fractions of the YSZ after exposure to the different environments. The refinement employed a four phase model that consisted of a *t'* and tetragonal phase with a space group of $P4_2/nmc$ [22], a cubic phase with a space group of $Fm\bar{3}m$ [23], and a monoclinic phase with a space group of $P2_1/c$ [23]. The *t''* phase discussed elsewhere [23] was not included in the fitting because it is not expected to form upon cooling from an aging temperature of 1330°C. A pseudo-Voigt function that incorporates asymmetry and strain broadening was used to fit the peak profiles as described by Thompson, *et al.* [24]. The displacement

parameters used in the model were obtained from Howard and Hill [25] and were fixed throughout the refinement.

Results and Discussion – The XRD peaks for the dry and humid aged condition up to a LMP of 15.2 K (88 h) are shown in **Figure 3** with the *t'*, tetragonal, and cubic peaks superimposed. All aging conditions look indistinguishable up to 15.2 K (88 h), for both the dry and humid aging conditions. It is notable though, that as the aging time increases for both environmental conditions the peak positions gradually shift away from the *t'* phase and towards the tetragonal and cubic phases.

Figure 4 shows the XRD results for the aging of the APS 8YSZ in both dry and humid environments for 15.2 K (88 h) to 18.2 K (570 h) of aging. A trend of increased monoclinic formation for the humid-aged sample relative to the dry one occurs from 15.9 K (140 h) to 18.2 K (570 h) of aging. However, the monoclinic formation is not the only change that is observed in the evolution of the phases during aging. There are also clear differences in the amount of cubic phase that is formed during the aging. In the humid environment, there is a decrease in the *t'* phase as the amount of the cubic phase increases. The amount of the tetragonal phase is also decreased in the humid environment due to the increased monoclinic formation.

Raman spectra of the as-received and aged APS 8YSZ are shown in **Figure 5**. The six characteristic Raman modes of tetragonal zirconia can be identified in the as-received condition, as well as in samples aged from 10.9 K (6 h) through 15.2 K (88 h) in both humid and dry environments. After aging in both environments, the initial width of the peak at 260 cm^{-1} narrows and the peak intensity ratio of the 640 cm^{-1} peak to the 260 cm^{-1} peak decreases relative to the as-received condition. There are no observable differences in the peaks obtained for the two aging environments up to 15.2 K (88 h) exposure times (where the spectra for the dry and humid conditions have been offset in **Figure 5** only to avoid overlap of the spectra). However, starting at 15.9 K (140 h) there are many additional peaks in the Raman spectra for the humid-aging condition that are not observed in the dry-aging condition. These peaks are identified as the characteristic monoclinic peaks, and the intensities of these monoclinic peaks grow relative to the tetragonal peaks with further humid aging to 16.7 K (224 h). At this aging time, there are still no discernible monoclinic peaks that can be identified for the dry-aging condition. These Raman spectra results correlate well with the XRD spectra in that there is an increase in the amount of monoclinic phase formed in the samples after a LMP of 15.9 K (88 h) under exposure to the humid environment.

Figure 6 shows a comparison of the XRD experimental data for the 16.7 K (224 h) dry- and humid-aged samples to the GSAS model. A quantitative metric for the quality of fit – the weighted profile R value called R_{wp} – gave a value less than 7.0% for both environments, which is consistent with the expectations for a Rietveld fit on data taken from conventional XRD equipment (a R_{wp} of ~10%) [26]. Visual inspection of the quality-of-fit shows that the model accurately reflects both the locations of the peaks, as well as the relative peak intensities – indicating that both the lattice parameters and the atom positions of the model are quite accurate. At 16.7 K (224 h) of aging, there are clear differences in the shape and intensities of the peaks for the different aging environments. This is mostly due to the reduction of the *t'*, tetragonal, and cubic phases in favor of the increased growth of the monoclinic phase in the humid environment.

Figure 7 shows the average phase fraction values and standard deviations from the Rietveld analysis performed on XRD spectra from the top, bottom, and polished-top of the 15.2 K (88 h) dry- and humid-aged 8YSZ samples. This was done in order to verify that the enhanced decomposition of the *t'* phase in the humid environment was not a result of yttria volatilization. The "top" refers to the side that faces up when placed in the crucible for aging testing and has a larger roughness than the reverse side – i.e. the "bottom" which is in contact with the loose yttria powder. The "polished-top" refers to a separate sample from the same test that had its top side polished down to P2400 grit size with SiC grinding papers prior to the tube furnace exposure. Two of these samples were run in each aging environment. All XRD spectra of the different surfaces were taken at the same dwell time and step size. For the Rietveld analysis, the same macro was used to determine the phase fractions of each XRD spectrum. The standard deviations for all

phase fractions shown are less than 0.015. The differences in the phase fraction values between the aging environments are greater than the standard deviations for three out of the four phases – the exception being the cubic phase. Therefore, the 15.2 K (88 h) humid-aged sample resulted in a faster decomposition of the *t'* phase compared to that of the dry-aged sample and is accompanied by a larger increase in the tetragonal and monoclinic phase fractions. Since the partial pressure of oxygen difference will be non-negligible between the "top" and "bottom" surface in contact with the loose yttria powder, it appears unlikely that volatilization of yttria is the means for the enhanced decomposition of the *t'* phase in humid environments.

The evolution of the GSAS-calculated phase fractions of the samples as they age in the different environments is shown in **Figure 8**. As the samples age in both environments, the *t'* phase decreases and the tetragonal, cubic, and monoclinic phases increase with increasing LMP up to 15.2 K (88 h) as expected. The *t''* phase was not included in the Rietveld refinement as it is not expected to form at temperatures around 1330°C [3]. Differences in phase fractions between the environments are slight until a LMP of 13.8 K (37.2 h), where there are noticeable differences in the amount of the cubic and tetragonal phases formed and the amount of the *t'* phase that has been decomposed. At this LMP the amount of the *t'* phase has decreased for the humid environment and the amount of the cubic and tetragonal phases have increased relative to the dry environment. The trend of the increased decomposition of the *t'* phase to the equilibrium phases for the humid-aging condition continues up to a LMP of 15.2 K (88 h) – prior to significant increases in the monoclinic phase. After 15.2 K (88 h), the trend is different because the tetragonal phase starts to decrease in both environments – more rapidly for the humid environment. This is expected as the monoclinic phase starts to increase significantly at this point for both environments – again at an accelerated rate for the humid environment. The cubic phase trend changes as well, with the humid environment forming less of the cubic phase than the dry one after 15.2 K (88 h). The decrease in the cubic phase formation for the final aging time in the humid environment is consistent with the work from Lipkin. *et al*. [3], where the amount of the cubic phase decreases for a subsequent aging time at large non-dimensional aging parameters. The one trend that continues after a LMP of 15.2 K (88 h) is the accelerated decomposition of the *t'* phase in the humid environment relative to the dry one.

Figure 9 shows the results for fitting the A_{1g} mode of tetragonal zirconia at the 259 cm^{-1} line for both the dry- and humid-aged YSZ. From 10.9 K (6 h) to 15.2 K (88 h), the 259 cm^{-1} line shifts to higher wavenumbers, but there is little difference in the peak shifting between the different aging environments at these LMPs. However, with continued aging to 15.9 K (140 h), the 259 cm^{-1} line shifts to a higher wavenumber for the humid environment relative to the dry. This increased amount of shifting for the humid aging continues for the longer exposure times of 16.7 K (224 h) and 18.2 K (570 h).

Figure 10 shows a comparison of the XRD spectra for a 16.7 K (224 h), humid-aged sample that was cooled in the humid environment as well a sample that was aged for 219.5 h in a humid environment, purged of the humid environment for 2.25 h at the aging temperature, aged for 2.25 h in a dry environment, and then cooled in a dry environment. The entire length of aging for this hybrid test was still 224 h (termed *hybrid 224 h* hereafter). The purpose of the *hybrid 224 h* test was to determine whether the monoclinic phase was forming only due to cooling in a humid environment at temperatures less than 400 °C. This transformation of the tetragonal phase to the monoclinic phase occurs at temperatures between 120-300°C in a humid environment due to LTD [15]. Therefore, to confirm that LTD was not the mechanism for the formation of the monoclinic phase in the humid aged sample, the *hybrid 224 h* test was performed. The 2.25 h purge was performed to ensure that the environment transitioned from one with 45% vol. of water vapor to one with no partial pressure of water vapor. The additional 2.25 h of dry heating was done so that the resulting XRD spectrum would reflect slight differences in the degree of phase evolution. The XRD spectrum comparison shown in **Figure 10** indeed confirms that the aging was not purely in a humid environment. **Figure 10** shows a difference in the amount of the monoclinic phase formed – (b) – and the evolution of the *t'* phase – (c). In addition, the presence of the monoclinic phase in the XRD spectra of the *hybrid 224 h* test confirms that LTD is not the means of the monoclinic formation, but is instead due to the conversion of the *t'* phase

to the tetragonal phase at the aging temperature – which is then converted to the monoclinic phase by the martensitic transformation [3].

In order to understand the enhanced destabilization of the *t'* phase of 8YSZ in humid environments at high temperatures it is illustrative to examine the diffusion paths of yttrium in the APS microstructure. Previously two possible diffusion paths of yttrium in dry, elevated aging temperatures were postulated for the complex microstructure of APS [4]. The first path is based on the coarsening of the Y-rich and Y-lean domains (Modulated Path), and the second path is dominated by the coarsening and growth of the cubic phase via depletion of Y from the tetragonal grains (Depletion Path). Both paths were thought to be present in the APS microstructure if there was inhomogeneity in grain size of the initial deposited 8YSZ. The juxtaposition of a large grain next to several small grains would cause equiaxed cubic grains to nucleate at grain boundaries due to the Depletion Path. Once the equiaxed grains are established, the Modulated Path would destabilize the *t'* phase of the adjacent larger grain by the presence of the Y-rich and Y-lean domains. The authors suggested that a larger initial grain size would increase the resistance of the tetragonal to the monoclinic transformation. However, this is at odds with the LTD in humid environments literature that has found that smaller initial grain sizes decreased the tetragonal to monoclinic transformation [9,14]. This conflicting understanding may in part be explained by differences in destabilization between the *t'* and tetragonal phase. Jue *et al.* [27] found that the *t'* phase had superior resistance to the monoclinic phase transformation than the 3-mol%-yttria tetragonal zirconia – with no monoclinic phase formation after 1000 h at 275°C in air. This is despite the fact that the *t'* polycrystalline material had a large grain size of ~100 um. The authors attributed the difference in resistance between the *t'* and the tetragonal zirconia to differences in the ferroelastic domain size, with the smaller domains of the *t'* phase providing higher resistance. Therefore, it seems unlikely then that the grain size alone is a factor in the destabilization of the *t'* phase in APS 8YSZ.

The quantitative Raman spectroscopy analysis provides evidence that the humid environment is enhancing yttrium diffusion after the formation of the monoclinic phase. Raman spectroscopy was used by Lee *et al.* [34] to show the influence of dopant concentration on the shifting of two characteristic, tetragonal Raman modes – one at 259 cm^{-1} and the second at 609 and 640 cm^{-1}. These two modes were singled out among the six tetragonal modes because they are believed to relate directly to the stretching of the two Zr-O bond lengths [34]. Different trends in the shifting of these Raman modes were found based on whether the dopant had an ionic radius that was oversized or undersized relative to zirconium. As the concentration of the oversized-dopant Ce^{4+} decreased in zirconia, the two Raman modes shifted to a higher wavenumber. Y^{3+} is an oversized dopant as well relative to the zirconium ion and should shift the two Raman modes in a similar manner as the Ce^{4+} ion. Peak fitting of the 259 cm^{-1} Raman mode – as shown in **Figure 9** – indicates that aging of the APS 8YSZ in either environment agrees with the previous findings that a decrease in an oversized dopant causes the wavenumber to shift to a higher value. This indicates that yttrium is leaving the *t'*-parent phase during aging in either environment. However, the fitting also indicates that the shifting to a larger wavenumber is occurring faster for the humid-aged samples than for the dry-aged samples – after the formation of the monoclinic phase. Therefore, the diffusion of yttrium is enhanced by aging in the humid environment after the formation of the monoclinic phase in 8YSZ.

The shifting of the Raman tetragonal modes provides strong evidence that yttrium is leaving the *t'* phase at an accelerated rate in a high-temperature, humid environment, but the role of impurities in enhancing the diffusion of yttrium during humid-aging is unclear. Impurities in commercially available 8YSZ powders were found to play a large role in cation diffusion pathways during the annealing of the powders. Heuer, *et al.* [36] identified an amorphous, silicate phase that was continuous along grain boundaries post-annealing by TEM imaging. This glassy phase was proposed to dissolve the parent microstructure and deposit a yttria-enriched precipitate free zone. A more recent analysis by Krogstad, *et al.* [4] also found pockets of silica at grain boundaries in APS 8YSZ after aging these materials in air. Silica impurities are also likely present in the APS 8YSZ used here and are expected to have a role in cation

diffusion. The question that arises is how do water species affect the silica impurities in enhancing yttrium diffusion? Davis, *et al.* [11] investigated the effect of varying Si content – from 56 to 760 ppm – on the LTD of zirconia with different yttria compositions in water vapor at 250°C. Although the authors had hypothesized that water vapor would react with the glassy silicates in a stress corrosion mechanism, the authors found no differences in the samples after aging despite the significant variation in Si content.

At temperatures relevant to this study, it is anticipated that some of the silica impurities in APS 8YSZ would volatilize as hydroxyl groups. Jacobson, *et al.* [37] confirmed that silica will volatilize primarily as $Si(OH)_4$ at 1300°C and at a partial pressure of 0.5 bar H_2O – conditions similar to the humid conditions utilized in this study. Therefore, while a glassy silicate phase is important as a yttrium diffusion pathway during the high-temperature aging of APS 8YSZ, it is not likely to enhance the diffusion of yttrium in a humid environments relative to a dry one. The detailed role of silica impurities and microstructure on the humid aging of APS 8YSZ is currently being investigated by a TEM analysis.

The role of proton or hydroxyl group migration on yttrium diffusion is unknown at elevated temperatures and not well understood in LTD. The diffusion profiles of Duong *et al*. [18] for the water derived species into single crystal tetragonal and cubic YSZ did not include Y. However, the authors noted that like Zr, the Y profiles were constant with depth indicating that the evolving depth profiles of H or deuterium (D) were independent of Y content. It is noteworthy though, that the isotope markers for H or D did not appear to diffuse into the cubic YSZ while it did for the tetragonal YSZ. This was surprising given that the higher Y content cubic phase has a higher oxygen vacancy content and many LTD papers have attributed the LTD mechanism to be governed by oxygen vacancy diffusion [9,38]. Therefore, one would expect an increase in the H or D diffusion into cubic YSZ but this was not observed. The authors explained the lack of H or D diffusion by either sluggish H_2O decomposition kinetics or by the higher Y content altering the energy landscape of H and D in zirconia.

A more recent analysis by Kiho *et al*. [39] performed a time-of-flight (TOF)-SIMS analysis on YSZ that was prepared by atomic layer deposition (ALD). ^2H_2O was used as the oxidant in the ALD process at 250°C in order to determine if protons could be incorporated into 50 nm films of YSZ that had variable amounts of yttria in it. A linear correlation between the relative concentrations of the Y^{3+} and $^2H^+$ ions was observed. Notably, the amount of D detected was the least in a pure zirconia sample as compared to samples with Y_2O_3 dopant. Furthermore, $Y(OH)_3$ was detected in the films by XPS which the authors proposed was formed due to Y^{3+} ions causing the chemisorption of water during ALD. The correlation of Y^{3+} and $^2H^+$ ions is at odds with the results found from Duong *et al*. [18] where the increased Y content of the cubic phase resulted in no diffusion of D. The discrepancy could perhaps be that Duong *et al*. [18] ignored the D and H profiles within the first 200 nm of the material due to irreproducible results, while the entire film investigated by Kiho *et al*. [39] was 50 nm in thickness. However, this does not provide any overall conclusion for the influence of protons on Y diffusion.

Even if there was a consensus on the role of protons in Y diffusion during LTD, it would likely be different from the scenario at elevated temperatures. The diffusion of cations in YSZ is known to be slow even at elevated temperatures. For example, it was estimated that it would take 7 years for Zr to travel 3 um at a temperature of 1200°C [40]. Therefore, at temperatures relevant to LTD (i.e. less than 400 °C) the Y diffusion is negligible while the distance at which Y will migrate at temperatures used in this study (i.e., 1330 °C) will still be small but significant relative to that of LTD. Also, the equilibrium phases are very different for the LTD conditions as compared with those of the high temperature, humid aging. For LTD conditions, a typical tetragonal concentration of 6 mol% $YO_{1.5}$ would make the equilibrium phases the monoclinic and cubic phases. Therefore, when placed in a humid environment, the tetragonal phase can be "destabilized" into the equilibrium phase by water-derived species diffusing into the YSZ lattice. The destabilization is believed to be occurring by either tensile stresses being generated in the grains by the species diffusion [38] and/or by reducing the amount of oxygen around Zr cations. The kinetics of this

destabilization are similar to that of oxygen vacancy diffusion implying that the activation energy of the LTD diffusing species is close to that of oxygen vacancy diffusion [15]. However, for high temperature, humid environments the *t'* phase falls within the tetragonal + cubic phase field. In order for the monoclinic phase to form, the *t'* phase has to undergo significant phase partitioning into the Y-lean and Y-rich equilibrium phases.

A key consideration is then what controls the rate of yttrium redistribution, and hence the development and coarsening of Y-lean and Y-rich domains. In a comprehensive study of lattice diffusion kinetics in yttria-stabilized zirconia [41], Chien and Heuer found that charged *defect clusters*, namely $\left(V_O^{\bullet\bullet} V_{Zr}^{''''}\right)''$, were rate controlling. Furthermore, these defect clusters would experience attractive interactions with oppositely charged defects such as isolated $V_O^{\bullet\bullet}$ and $\left(Y_{Zr}' V_O^{\bullet\bullet}\right)^{\bullet}$, and repulsive interactions with similarly charged defects such as Y_{Zr}' – both of which reduce the mobilities of the rate controlling defect clusters, and hence the migrating cations. In this analysis, the oppositely charged defects, $V_O^{\bullet\bullet}$ and $\left(Y_{Zr}' V_O^{\bullet\bullet}\right)^{\bullet}$, are identified as diffusion-trapping centers, while like-charged Y_{Zr}' and the neutral defect clusters $\left(2Y_{Zr}' V_O^{\bullet\bullet}\right)^{X}$ and $\left(2V_O^{\bullet\bullet} V_{Zr}^{''''}\right)^{X}$ are identified as diffusion-blocking centers. A key observation in this work was that the diffusivity in 18 mol% Y_2O_3 doped zirconia was approximately one-fifteenth that in 9.4 mol% Y_2O_3 material, contrary to what might be expected with higher doping levels providing for a higher defect density. The authors conclude that the observed slower diffusivity was due to the higher defect density of trapping and blocking centers in the 18 mol% zirconia, in relation to the 9.4 mol% material.

Once the partitioning of the equilibrium phases occurs, the tetragonal phase has been proposed to be kinetically limited to transforming to the monoclinic phase upon cooling due to coherency strains that exists at the interfaces between ferroelastic domains [31]. Evidence for these coherency strains due to the high temperature dry aging of the *t'* has been found by the shifting of Raman lines [5] and by the approximation of strain by XRD analysis [7]. These coherency strains arise with thermal aging once yttrium partitioning takes place producing domains that are coherently bound but have different lattice parameters. This partitioning can occur within an hour of aging time at temperatures of 1482°C [7]. When the domains are at the nanoscale, they are fully coherent and prevent the Y-rich and Y-lean phases from relaxing to their equilibrium lattice parameters. The small diffusion distances of Y were found to be of the same order as that of the domains implying that Y partitioning is dictated in part by the coherency strain contribution [7]. As coherent phases will have an associated larger Gibbs free energy than incoherent phases, the domains are thermodynamically driven to coarsen and become incoherent. The coherency strain can therefore help explain how the tetragonal phase is prevented from transforming into the monoclinic phase even though it is predicted by the phase diagram. The proposed role of coherency strains in limiting Y redistribution during the high temperature aging of the *t'* phase is not a factor in the LTD mechanism because the parent phase is fully tetragonal and cannot be partitioned into Y-rich and Y-lean phases. However, the coherency strains are proposed to have a key role in understanding the phase evolution during the high temperature, humid aging of the *t'* phase as will be explained in the next section.

The question of how exposure to elevated water vapor content in the high temperature service environment may influence the aging, and destabilization of the YSZ emerges as the primary concern underpinning the current work. As explored in the following, the enhanced destabilization of the *t'* phase in high temperature, humid environments may be related to proton incorporation, and an enhanced ability to overcome the coherency strains that exist between the tetragonal and cubic domains in 8YSZ.

Exposure to steam environments can incorporate protons into 8YSZ in a similar manner as that which was proposed by Prinz *et al*. [20], where water is dissociated and interacts with anion vacancies, forming charged hydroxyl groups situated on anion sites:

$$H_2O + V_O^{\bullet\bullet} + O_O^X \xrightarrow{YSZ} 2(OH)_O^{\bullet} \quad (1)$$

While lattice diffusion of these ions is possible, it is more energetically favorable for them to travel along splat/grain boundaries [16]. The oxygen anions are not anticipated to have a dominant effect here in destabilizing the tetragonal phase as they do in LTD. This is due to the fact that the enhanced destabilization is occurring at a temperature where the tetragonal phase is at equilibrium for 8YSZ as opposed to LTD where the monoclinic phase is at equilibrium. However, proton incorporation and migration in the 8YSZ is likely to play a more pivotal role in the high temperature, humid degradation. Although historically YSZ has not been considered a proton-conductor, recent computational studies support the incorporation and long-range transport of protons in YSZ by "hopping" between closely spaced oxygen ions [16,17]. Furthermore, evidence of proton incorporation via the formation of hydroxyl groups has also been demonstrated in YSZ thin films at temperatures below 450°C [19,20]. As such, there is theoretical and experimental support for protons to be incorporated into the structure of YSZ and influence the destabilization of the tetragonal phase.

However, the fact that there is a delay in seeing the monoclinic phase or significant changes in the evolution of the *t'* phase at exposure times less than 15.9 K (140 h) for the humid environment suggests the presence of an incubation period that needs to be surpassed prior to the tetragonal phase transforming into the monoclinic phase. This incubation period is likely linked to the coherently strained interfaces that develop between the tetragonal and cubic phases in the aging of 8YSZ [7]. A humid environment may decrease the incubation time by changing the defect chemistry of the evolving material. In reference to the defect reaction shown above, equation (1), water vapor may result in a conversion of oxygen anion sites to hydroxyl groups via the proton "hopping" mechanism, with attendant elimination of oxygen vacancies. A side effect of the conversion of oxygen anions to hydroxyl groups is a reduction of the effective size of these lattice sites. The 'smaller' hydroxyl groups would allow for a larger displacement of the oxygen atoms along the c-axis – or an increase in the tetragonality. This would explain the increased formation of the tetragonal phase during humid aging observed in the Rietveld refinement results of **Figure 8**.

In reference to the study by Chien and Heuer [41], the role of water-derived species may not be just in interacting with isolated oxygen vacancies at high temperatures, but rather with *defect clusters* instead. Given the complex defect chemistry of yttria-stabilized zirconia, it is possible that aging in a humid environment may affect the concentrations of diffusion-trapping and diffusion-blocking defects. The implication is that cation mobility – and therefore the kinetics of domain coarsening – may be enhanced. With enhanced coarsening, the interfacial coherency strains that exist at the boundaries between Y-rich and Y-lean domains may be overcome faster. This enhanced coarsening rate would ultimately cause the domains to become incoherent, and thereby allow the tetragonal phase to become susceptible to monoclinic transformation faster.

Additionally, there is the possibility that a high temperature, humid environment could be changing the metastable phase boundary line shown in **Figure 1**, and thus modifying the change in Gibbs free energy associated with the tetragonal and monoclinic phases. However, if there is enhanced domain coarsening for the humid aged samples, this would indicate that differences are occurring between the different environments while at the aging temperature. This would in turn reduce the role of a shifting metastable phase boundary line in the enhanced destabilization of the *t'* phase – however at this point, it can't be ruled out as a possible mechanism. A microstructural evolution investigation is currently under way to determine if there is, in fact, an enhanced coarsening of the domain size in humid environments.

Conclusions **–** The high-temperature, humid aging of APS 8YSZ has shown an accelerated de-stabilization of the *t'* phase compared to that of observed with dry environment exposure. X-ray diffraction measurements and Raman spectroscopy show a similar decomposition of the *t'* phase to the thermodynamically stable cubic and tetragonal phases up to LMP = 15.2 K (88 h) of aging at 1330°C. However, after 15.9 K (140 h) of aging, the amount of the monoclinic phase has increased in the humid environment relative to that observed with a dry environment exposure. The mechanism by which the monoclinic transformation is accelerated is possibly associated with the incorporation of protons via

hydroxyl group formation. The hopping of such protons at neighboring oxygen sites would cause these sites to become smaller and allow them to relax to their equilibrium positions faster. Such an increase in tetragonality may allow the coherency strains between bound cubic and tetragonal phases to be overcome faster in a humid environment. The tetragonal phases could thus coarsen faster and reach a size that would cause the monoclinic phase to nucleate faster in this humid environment. Alternatively, the incorporation of water-derived species may affect the overall defect chemistry, reducing the concentrations of diffusion-trapping and diffusion-blocking defects and increasing the kinetics of yttrium redistribution – and therefore the overall Y-rich and Y-lean domain coarsening. The revelation of accelerated monoclinic phase transformation of the *t'* phase by high temperature, humid aging should promote a better understanding of the expected durability of APS 8YSZ coatings used in power generation gas turbines with high-hydrogen content fuels.

3. Aging of Yttria-Stabilized and Dysprosia-Stabilized Zirconia Based Abradable Coating Systems

Given the previous findings that the matrix material comprising the abradable coating system is susceptible to enhanced degradation in elevated water vapor environments, the effort then turned toward exploring the behavior of representative ceramic abradable coating systems. The primary focus was on evaluating the microstructural evolution that occurs in low and high water vapor exposures, and assessing how that might effect durability and abradable performance.

Approach **–** The performance of the abradable coatings in a representative working environment was examined using a high temperature, controlled atmosphere tube furnace. A mullite tube was used since it has higher resistance to thermal shock than alumina. A mixture of nitrogen and oxygen at a ratio of 80:20 and a flow rate of 80sccm was first fed through a heated water tank before entering the tube furnace. The temperature of the water tank controlled the amount of water vapor in the atmosphere that was flowed across the sample. For a water vapor percentage by partial pressure of 9.5% H_2O (v), which was representative of natural gas fired turbines, the tank was heated to 45˚C [2]. Additionally, the inlet tubes and flanges are wrapped in heating tapes and heated to >100˚C to ensure no water condensed in the tube. The furnace set up is shown in **Figure 11**. Prior to starting the furnace program and after the water tank had reached the set temperature, the gas flow was turned on and the system was purged in a wet environment for two residence cycles at a furnace and heating tape temperature of 150˚C. The furnace program was then started, and the coatings were exposed to 9.5% or 30% H_2O (v) at 1100˚C with a 10˚C/minute ramp rate for 10-145 hours.

Two commercially available APS ceramic abradable systems were studied. The first was a dysprosia stabilized zirconia (DySZ), polymer, hBN system (further referred to as DySZPB). The second was a YSZ, polymer abradable system. DySZPB coatings were processed by air plasma spray at two different suppliers, Plasma Technology Incorporated and Solar Turbines Incorporated, using Durabrade 2192 spray dried powders purchased from Oerlikon Metco US Inc. These coatings are further referred to as DySZPB (processed by PlasmaTech.) or DySZPB_ST (processed by Solar Turbines). The APS YSZ, polymer system was sprayed by both suppliers as well using Metco 2460NS spray dried powders also purchased from Oerlikon Metco. The 2460NS coatings are further referred to as YSZP (processed by PlasmaTech.) or YSZP_ST (processed by Solar Turbines). Powder specifications are listed in **Table I**. Two important differences to note in the starting powders are different starting powder morphologies and lower percentage of dysprosia stabilizer by mole percentage used in the DySZPB coating specimens. The thermally sprayed preparations produced the types of samples shown in **Figure 12** and **Figure 13**.

Two bulk material compositions, YSZ and a YSZ-hBN composite, were also processed to study the matrix material behavior without the additional defects inherent to the APS process. Tetragonal 4 mol% YSZ (4YSZ) samples were made using Tosoh Corporation TZ-4Y powders (>99.8% purity, 40nm particle size). Both tetragonal (t) and the metastable phase, tetragonal prime (t'), bulk YSZ materials were processed. The

tetragonal, t 4YSZ, was made by first pressing the powders at 7 tonnes for 5 minutes. It was then sintered in air at 1250˚C for 18 hours with a 10˚C/min. heating and cooling rate using a CM Furnaces Inc. 1700C tube furnace with a mullite tube.

The t' 4YSZ samples were processed using spark plasma sintering (SPS) with a Fuji SPS 825-S. For SPS, the 4YSZ powders were first weighed and loaded into 18 mm diameter graphite dies with 2 sheets of graphite foil. SPS parameters of 100˚C/minute heating rate, 65 MPa pressure, 1600˚C sintering temperature, 10 minute hold time, and 200-300˚C cooling rate were used. The temperature of the sample was monitored using an optical pyrometer, and the cooling rate was reached by shutting off the instrument and letting the sample cool to ambient temperature. The graphite foils on the SPS sintered samples were then ground off, and the samples were annealed in air at 900˚C for 8 hours with a 2˚C/minute heating rate and 10˚C/minute cooling rate.

In addition, a composite of the same Tosoh 4YSZ powders and 25 vol. % hBN was processed by first ball milling the powders in ethanol using 5 mm diameter zirconia milling media. The ball mill was run at 40 rpm for 12 hours. The milled powders were then dried and ground using a mortar and pestle. Polyvinyl alcohol (PVA) was added as a binder to the 4YSZ-hBN composite powders prior to pressing to assist homogeneous compaction of these powders into green bodies. PVA at 3 vol. % was added to the 4YSZ-hBN powders by first dissolving the PVA binder in distilled water at 80˚C. The 4YSZ-hBN powders were then added with continuous stirring. The PVA, 4YSZ, hBN powders were dried at 110˚C overnight then ground with a mortar and pestle. Green bodies of each composition were then pressed and heat treated at 450˚C for 8 hours with a 5˚C/min. ramp rate to remove the polymer. The 4YSZ-hBN composite was then sintered in nitrogen at 1365˚C for 12.5 hours with a 10˚C/min. heating and cooling rate.

Coating samples were prepared for characterization and testing by first polishing off any underlying substrate and bond coat material on the APS coatings to make free-standing coatings. The as received coatings, which were around 760 µm thick, were then heat treated to remove the polymer pore former at 450˚C for 8 hours with a 5˚C/minute ramp rate as suggested by the powder manufacturer. Both the coatings as well as bulk material samples were then cut using a high-speed diamond blade, mounted in epoxy, and polished to a 0.25 µm finish.

Polished samples were coated with iridium or carbon to prepare for scanning electron microscopy (SEM) imaging in a FEI Magellan Field Emission Gun SEM to determine the microstructure of the samples. ImageJ analysis software was used to analyze the area fraction of the porosity and secondary phase. Rough polished samples were used for Raman spectroscopy with a 532 nm laser on a Renishaw inVia Raman Microscope to analyze the hBN phase (< 1 wt. %) in the coatings. Powder x-ray diffraction (XRD) was performed on a Rigaku Corporation Ultima III X-ray Diffractometer with a Cu k-alpha source, 1.54 Å wavelength to confirm the t' phase and to analyze the hBN phase in the bulk materials.

In addition to characterization and testing of as processed materials, aging experiments were carried out on the free-standing APS coatings to replicate microstructural changes seen with increasing operational time in the turbine. Aging experiments were completed using a high temperature, controlled atmosphere tube furnace. To test in a representative natural gas fired turbine combustion stream, 9.5% H_2O (v) by partial pressure in a mixture of nitrogen and oxygen gas at a ratio of 80:20 and a flow rate of 80sccm were flowed across the sample surface for aging experiments. To test in a representative synthetic gas fired turbine combustion stream, 30% H_2O (v) by partial pressure in a mixture of nitrogen and oxygen gas at the same ratio and flow rate as above were used during aging experiments [2]. Aging was performed at 1100˚C with a 10˚C/min. ramp rate for hold times up to 145 hours. The tube furnace system was purged in the wet environment for two residence cycles at 150˚C prior to exposure.

Results and Discussion: As-Received Characterization **– Figure 14** shows the as received microstructures of the bulk t YSZ, t' YSZ (fracture surface), and YSZ-hBN samples. Bulk t and t' YSZ as well as YSZ-

hBN are >98% dense with >1μm grain sizes, and the composite contains the expected 30 vol. % of hBN, confirmed by image analysis and x-ray diffraction, shown in **Figure 15**. It is evident that in addition to the tetragonal YSZ and hBN phases, there is also an additional oxidized zirconium boride phase, shown in literature with high pressure synthesis [42,43]. The t' phase in the 4YSZ processed by SPS was confirmed using XRD, as shown in **Figure 16**.

Figure 17 shows the YSZP and DySZPB APS coating materials processed by both suppliers. The APS coatings, YSZP_ST and DySZPB, have 34% and 27% porosity, respectively, which was analyzed by area fraction. The DySZPB_ST coating contained a much lower porosity percentage at 12%, and the YSZP coating showed inhomogeneous distribution of porosity through the thickness, evident in the denser surface of the coating shown in **Figure 17**, of YSZP. Because the porosity distribution and percentage was most similar in the YSZP_ST and DySZPB coatings, this study focused on those systems.

Upon closer SEM examination of the YSZP coatings, the presence of 'nanozone' features is evident in both YSZP coatings, as shown in **Figure 18**. These nanozones are created during the spray process as partially unmolten particles remain after being sprayed onto the surface. YSZ coatings with nanozones are well documented in the literature when using nano-agglomerated spray dried powders [44,45]. The YSZP_ST coatings contain around 8% nanozones by area.

Raman spectroscopy was used on the DySZPB coatings in order to verify the structure of the BN phase in the as processed state. **Figure 19** shows the Raman spectra of the Durabrade 2192 powders and the processed coating with the absence of the characteristic E_{2g} peak for hBN in the APS coating [46]. Further examination was done by Raman spectroscopy on the DySZPB_ST coating processed by a different supplier than DySZPB, confirming the absence of the peak at 1367 cm^{-1}. The DySZPB coatings were also investigated by transmission electron microscopy, which showed the presence of an amorphous form of BN as seen in **Figure 20**. Raman spectroscopy of aged DySZPB coatings also showed an absence of the hBN peak.

Results and Discussion: Aging Studies **– Figure 21** and **Figure 22** show SEM micrographs of the evolution of the APS coatings under simulated natural gas, 9.5% H_2O (v), and synthetic gas, 30% H_2O (v), turbine combustion atmospheres. With increasingly longer exposures at both low and high water vapor contents, the YSZP_ST and DySZPB coatings both undergo densification leading to a decrease in concentration of open APS splat boundaries. It is particularly evident in the DySZPB coatings, shown in **Figure 21**, with extensive closing of the open splat boundaries seen in the SEM micrographs starting at the lowest exposure time of 10 hours. The YSZP_ST coatings, on the other hand, don't show the same extent of open splat boundary closing, but do show evidence of sintering. **Figure 23** shows a comparison of the YSZP_ST and DySZPB coatings exposed for 145 hours in high water vapor at higher magnification to illustrate the difference in the extent of sintering between the two coatings.

Image analysis with lower magnification images of the overall porosity percentage, including coarse, fine, and intrasplat porosity, in the YSZP_ST coatings at 9.5% H_2O (v) changes from 34.4 +/- 1.8% in the as received to 32.5 +/- 1.6% for the 145 hour exposure. The total porosity in the DySZPB coatings at 9.5% H_2O (v) changes from 27.1 +/- 2.6% for the as received to 25.4 +/- 2.9% for the 145 hour exposure. There is no significant change in the YSZP_ST overall porosity percentage in higher water vapor versus low at 145 hour exposure, but the DySZPB coatings show an increase in overall porosity percentage to 31.6 +/- 2.5% in high water vapor at 145 hours. This increase in porosity seen in DySZPB from low to high water vapor is due to the oxidation, volatilization reaction of BN being enhanced in a higher water vapor environment and overshadowing the reduction of porosity expected with sintering. The expected reactions of the BN would proceed according to the following reactions [47].

$$4\ BN\ (s) + 3\ O_2\ (g) \rightarrow 2\ B_2O_3\ (l) + 2\ N_2\ (g)$$

$$B_2O_3\ (l) + H_2O\ (g) \rightarrow BOOH\ (g), B(OH)_3\ (g), (BOOH)_3\ (g)$$

Figure 24 shows SEM images of fracture surfaces of the DySZPB coatings, which gives insight into the densification mechanism, before and after exposure. In the micrographs looking at the low versus high water vapor aging experiments for each material, similar extents of intrasplat boundary removal are seen with no significant differences between the two at the same exposure time seen with the aging times used in this study. This intrasplat boundary removal occurs first by surface diffusion coarsening the intercolumnar grains within a splat. These coarsened grains then act as bridges across the APS splats thereby filling in the open splat boundaries. Densification of APS TBC materials by this bridging mechanism enabled by surface diffusion and further bulk diffusion above ~1000˚C has been well documented in the literature [48,49].

Discussion and Conclusions **–** Aging studies of both coating materials at conditions representative of two different combustion atmospheres have been shown. It was found that at a current hot section abradable coating working temperature of 1100˚C, densification is the main microstructure evolution that would affect the deformation behavior of the APS abradable coatings. For both low and high water vapor atmospheres used in exposures, the removal of open splat boundaries was seen with no significant difference in sintering seen between high and low water vapor tests at times up to 145 hours.

In addition, this study shows the difference in damage accommodation behavior between two current technology hot section ceramic abradable coatings as well as an evolution of damage mechanism type occurring with aging in the YSZP coating in particular. The two coatings studied in this work are representative of design strategies employed to modify existing ceramic coatings based on TBCs to enable abradability. Both coatings contain defects inherent to the APS process, such as splat features, intrasplat boundaries, fine porosity, microcracking, and columnar grains within a splat, as well as coarse porosity made using pore formers. The two coatings, however, differ with nanozone features present in the YSZP coating, while DySZPB contains BN, as a dislocating phase, and dysprosia as opposed to yttria as the zirconia stabilizer.

The expected benefit of the difference in the DySZPB coating of using a Dy_2O_3 stabilizer as opposed to Y_2O_3 is to lower thermal conductivity, which has been shown in DySZ TBC materials, and is important for abradable coatings that also provide a thermal barrier for the shroud [50,51]. Performance based testing of DySZPB and YSZP coatings, however, has shown further improved thermal cycling behavior and erosion resistance of the DySZPB coatings in comparison with YSZP [52]. This is likely due to the smaller mole percentage of stabilizer used in the DySZPB (3.3 mol. % DySZ) compared to YSZP (4.2 mol. % YSZ) and corresponding higher tetragonality of the unit cell, resulting in a more effective use of the t’ ferroelastic toughening mechanism present in both DySZ and YSZ materials [53-56]**.** The enhanced properties reported in literature for DySZPB over YSZP coatings are thus not attributed to an enhanced toughness or different toughening mechanism present in the matrix phase of DySZ versus YSZ, but are instead attributed to using a lower mole fraction of stabilizer in DySZPB.

For the additional secondary phase addition in the DySZPB coating, it was expected that the BN with a hexagonal, graphitic structure would act as a dislocating agent. This dislocating agent promotes abradability with the introduction of its weak bonding between basal planes. However, that expected behavior is challenged by the result in this study that the hexagonal structure is not maintained in the BN phase after APS processing. The amorphous form of BN present after processing nor its properties are known. Regardless, the lateral fracture dominated damage behavior in the DySZPB coatings with little extension through the coating thickness is more similar to the behavior seen in the damage zone of the bulk

YSZ-hBN composite. This is seen in all the DySZPB coatings despite the increased hardness and extensive densification evident in microstructures with aging, which suggests this secondary phase plays a role in maintaining a constant damage accommodation mechanism.

A final significant finding shown in this work is that increased hardness does not always signify a decrease in abradability, which is the current understanding in literature to date. The DySZPB coatings showed the most extensive densification and a larger than two fold increase in hardness with aging yet maintained a constant behavior with little damage accommodation extending deep within the material. The extent of densification in YSZP, however, does not cause a significant increase in hardness of the aged coatings. Yet, the damage accommodation behavior of the YSZP coatings changes at higher aging times. This signifies that hardness alone is not a good predictor of the ease of abradability because it is unable to give insight into the underlying damage accommodation mechanism for materials with a range of microstructural features.

4. Mechanical Testing and Evaluation of Abradable Materials

Abradable coating samples were tested for wear behavior using representative lab scale tests to simulate the combination of normal and shear loading experienced during service. Indentation tests were first used to evaluate the hardness of the coatings. It is known that as hardness increases, abradability decreases so the change in hardness of the DySZPB and the YSZP coatings will correlate to how the abradability of these coatings will evolve in service. To evaluate the wear characteristics, indentation scratch testing was used. Ideally, an abradability test rig simulating the impact of turbine blades at working impact velocities and temperature would be used. However, these rigs are currently only being run in industry and investigation into the feasibility of designing and building such a rig put those experiments out of the scope of this PhD project. Scratch testing was used as a comparative evaluation tool of the wear behavior of the exposed coatings although it is not a representation of coating wear behavior at working temperature. The mode of material removal during scratch testing can give insight into how the material will behave in service.

Approach: Hardness Testing – Bulk and APS coating materials were tested for hardness using Vicker's indentation with both as received and exposed coatings being tested. **Figure 25** shows the hardness of bulk t YSZ, t' YSZ, and the YSZ-hBN composite. The hardness of the composite is significantly lower than that of the bulk YSZ samples due to the hBN phase. **Figure 26** shows the hardness of the APS coatings as compared to a standard 7 wt. % YSZ TBC processed by APS for reference. With 145 hours of exposure to 1100˚C and 9.5% H_2O (v), the hardness of the DySZPB coatings increases to twice that of the as received coating while the YSZP abradable sees a negligible increase in hardness with aging.

Approach: Nanoindenter Scratch Testing – **Figure 27** shows representative progressive load scratches of as received DySZPB and YSZP_ST coatings performed by the nanoindenter. With progressive loading, wear mechanism transitions were expected along the length with the changes going from plowing to powder formation to flake formation with increasing contact pressure [57]. **Figure 28** illustrates the microcracking seen in the YSZP_ST scratch track where plowing has occurred. However, the characteristics along the length of the scratch tracks of both coating systems are variable, changing from plowing to extensive lateral fracture and flake formation then back to plowing. With SEM investigation, these multiple transitions did not correspond to any particular microstructural feature in the coating and was not consistent between several different scratches performed on the same material. The extent of indent depth and size variation in these regions along a scratch track is illustrated in **Figure 29**, and a 3D topography map from the optical

vibrometer is shown in **Figure 30** illustrating the extent of piled up material along the edges of the scratch track.

Figure 31 shows data for several YSZ-based APS coatings with change in displacement of the indenter tip into the coating as load is increased. Three scratch tests are shown on the YSZP_ST coating with test2 appearing to have a sudden increase in displacement with loads > ~250mN. This behavior was seen in multiple other tests on YSZP_ST as well as DySZPB coatings. Upon further SEM investigation of the scratch tracks exhibiting this behavior, it was evident that the indenter tip did not follow a straight path as it was applying load to the sample. **Figure 32** shows a scratch track representative of this behavior. It is expected that the stochastic nature of the APS coatings, the size of the indenter tip not being sufficiently larger than the APS microstructural features, as well as sensitivity of the instrument tip resulted in faulty scratch tests. There were no repeatable results in the coatings due to the fact that the scratch tracks were not straight and that the load was reduced by the machine as a safety mechanism when the indenter tip saw too much resistance from the material or lateral deflection during testing. First using a larger size indenter tip was investigated, but the Agilent G200 system in use had a maximum load of 500mN, and the associated pressure applied with a larger indenter tip would not have been sufficient enough to probe a depth larger than 1-2 splat length scales in the coating material. Thus, further testing was explored to accurately test the behavior of the coating materials and is discussed in the next section.

Approach: MicroScratch Testing **– Figure 33** shows representative cross sectional SEM images of the tracks made by macroscratch testing the bulk materials. The damage in the bulk t YSZ material is shown through median and radial cracking. The YSZ-hBN composite however, does not show the same crack extension into the material and has a much larger scratch track than YSZ. **Figure 34** shows SEM images of the surfaces of the macroscratched t YSZ vs t' YSZ bulk materials. It is evident in the t' YSZ that the scratch track was made by intergranular fracture, which is likely due to the SPS process at high temperatures and the corresponding large grain size. The same intergranular fracture was not observed in the t YSZ or YSZ-hBN bulk materials after macroscratch testing.

Figure 35 and **Figure 36** show topographical maps of bulk YSZ and YSZ-hBN scratch surfaces measured by an optical vibrometer. **Figure 35** shows the YSZ scratch track and dimensions of the track along the length. It is evident that along the scratch, there exists a main scratch trench as well as areas of chipping caused by the extension of lateral cracks to the surface. These chipped areas increase the area of the scratch track significantly, with the trenches being around 50µm in width and chipped areas over 200µm. The depth of the scratch track along the length also varies slightly but is mostly constant between 10-20µm. The scratch track for the bulk YSZ-hBN composite, shown in **Figure 36**, does not show chipping as seen in YSZ. The scratch maintains a width around 200µm and a depth of 35-45µm, larger than the YSZ due to the higher hardness of the bulk YSZ.

Approach: MacroScratch Testing **– Figure 33** shows representative cross sectional SEM images of the tracks made by macroscratch testing the bulk materials. The damage in the bulk t YSZ material is shown through median and radial cracking. The YSZ-hBN composite however, does not show the same crack extension into the material and has a much larger scratch track than YSZ. **Figure 34** shows SEM images of the surfaces of the macroscratched t-YSZ vs t'-YSZ bulk materials. It is evident in the t'-YSZ that the scratch track was made by intergranular fracture, which is likely due to the SPS process at high temperatures and the corresponding large grain size. The same intergranular fracture was not observed in the t-YSZ or YSZ-hBN bulk materials after macroscratch testing. **Figure 35** and **Figure 36** show topographical maps of bulk YSZ and YSZ-hBN scratch surfaces measured by an optical vibrometer. **Figure 35** shows the YSZ

scratch track and dimensions of the track along the length. It is evident that along the scratch, there exists a main scratch trench as well as areas of chipping caused by the extension of lateral cracks to the surface. These chipped areas increase the area of the scratch track significantly, with the trenches being around 50μm in width and chipped areas over 200μm. The depth of the scratch track along the length also varies slightly but is mostly constant between 10-20μm. The scratch track for the bulk YSZ-hBN composite, shown in **Figure 36**, does not show chipping as seen in YSZ. The scratch maintains a width around 200μm and a depth of 35-45μm, larger than the YSZ due to the higher hardness of the bulk YSZ.

Figure 37 and **Figure 38** show the optical vibrometer topographical maps of the scratch tracks for the as received YSZP and DySZPB abradable coatings. Both coating systems show similar trenches with chipping along the scratch track as seen in the bulk YSZ. Both systems also have significant changes in scratch track depths along the length likely due to the presence of coarse porosity in the coatings. The YSZP scratch depths vary from 50-120μm, while the DySZPB coatings vary in depth from around 15-70μm from the trench areas to the highly chipped sections. The YSZP scratch depths are larger than the DySZPB coatings due to the YSZP coatings having a lower hardness.

Cross sectional SEM images of the as received as well as aged YSZP and DySZPB coatings are shown in **Figure 39**. The as received YSZP coating as well as YSZP aged for 50 hours show a distinct damage zone that penetrates deep within the coating. It is characterized by a particulate-like microstructure where microcracks have broken up the APS splat microstructure, which is shown at higher magnification in **Figure 40** in comparison to the DySZPB coating. The YSZP coating aged for 145 hours, however, does not show the same damage zone microstructure and only shows the particulate-like structures near the surface. Multiple areas along the scratch were analyzed by polishing further into samples to ensure the behavior was representative. All DySZPB coatings also do not have the same microcrack penetration deep within the material. The progression of the DySZPB cross sections, however, does show a significant change in scratch track size with aging. The scratch track penetration depth and size becomes significantly smaller with longer aging times.

Results and Discussion – A first result of this study shows the efficacy of two different lab scale test strategies attempted for use in evaluating the deformation behavior of abradable coating materials using a highly tangential force. The first testing strategy was a microscratch test using a conical diamond tip with a nanoindenter in sliding mode. This ~5 μm in radius tip could be representative of deformation seen when abradable coatings interact with turbine blades that have been tipped with abrasive materials. The attempted progressive load testing, however, did not show the expected wear transitions in the YSZP and DySZPB APS coatings. This is attributed to the combination of highly stochastic microstructural features present in the APS coatings and the sensitivity of the instrument being too high to maintain a straight scratch track at the desired load range of 0-500mN. Using a higher stiffness indenter head or a higher load could have enhanced the efficacy of this method. However, maximum load limitations and indenter head options excluded this as a viable option leading to the implementation of the second macroscratch test setup, which utilized a Vicker's diamond tip indenter to scratch the coatings at a constant load. This setup employed a tip size significantly larger than the microstructural feature length scales present in the APS abradable coatings, which is more representative of the interaction of an abradable coating with an untipped blade.

Aging studies of both coating materials at conditions representative of two different combustion atmospheres have been shown. It was found that at a current hot section abradable coating working temperature of 1100˚C, densification is the main microstructure evolution that would affect the deformation behavior of the APS abradable coatings. For both low and high water vapor atmospheres used in exposures, the removal of open splat boundaries was seen with no significant difference in sintering seen between high and low water vapor tests at times up to 145 hours.

In addition, this study shows the difference in damage accommodation behavior between two current technology hot section ceramic abradable coatings as well as an evolution of damage mechanism type occurring with aging in the YSZP coating in particular. The two coatings studied in this work are representative of design strategies employed to modify existing ceramic coatings based on TBCs to enable abradability. Both coatings contain defects inherent to the APS process, such as splat features, intrasplat boundaries, fine porosity, microcracking, and columnar grains within a splat, as well as coarse porosity made using pore formers. The two coatings, however, differ with nanozone features present in the YSZP coating, while DySZPB contains BN, as a dislocating phase, and dysprosia as opposed to yttria as the zirconia stabilizer.

In the YSZP coatings, the additional presence of nanozone features, shown in literature to enhance abradability under certain conditions or even introduce plastic-like behavior to the coating, do not show the expected damage accommodation mechanism [45]. The as processed and YSZP coating aged for 50 hours show a large damage zone beneath the macroscratch track that extends deep within the coating. It is characteristic of a brittle fracture in the coating with a microcrack network penetrating the weak intercolumnar grains within a splat, thereby breaking up the APS splat features. A similar behavior of crack formation and propagation into the material is seen in the dense, bulk 4YSZ macroscratch damage zone. The highly intergranular fracture seen in the t' 4YSZ bulk material is attributed to the use of the SPS process and fast cooling rate, which produced high residual stress in the coating making it unsuitable for comparison. However, with 145 hours of exposure at 1100˚C and 9.5% H_2O (v), the damage behavior in the YSZP changes to a more lateral fracture with little damage seen beneath the scratch track. Literature studies on APS YSZ have shown that aging increases the modulus and fracture toughness as well as reduces the amount of APS defects present in the coating [58]. From studies on the wear of ceramics, it is known that the extent of lateral and radial cracking is mainly controlled by hardness and fracture toughness with low hardness and fracture toughness resulting in more radial and lateral cracking[59,60]. It is expected that the extent of densification in the YSZP coating aged for 145 hours was sufficient to increase the coating modulus and fracture toughness, which changed the observed damage behavior.

The expected benefit of the difference in the DySZPB coating of using a Dy_2O_3 stabilizer as opposed to Y_2O_3 is to lower thermal conductivity, which has been shown in DySZ TBC materials, and is important for abradable coatings that also provide a thermal barrier for the shroud[50,51]. Performance based testing of DySZPB and YSZP coatings, however, has shown further improved thermal cycling behavior and erosion resistance of the DySZPB coatings in comparison with YSZP [52]. This is likely due to the smaller mole percentage of stabilizer used in the DySZPB (3.3 mol. % DySZ) compared to YSZP (4.2 mol. % YSZ) and corresponding higher tetragonality of the unit cell, resulting in a more effective use of the t' ferroelastic toughening mechanism present in both DySZ and YSZ materials[53-55]**.** The enhanced properties reported in literature for DySZPB over YSZP coatings are thus not attributed to an enhanced toughness or different toughening mechanism present in the matrix phase of DySZ versus YSZ, but are instead attributed to using a lower mole fraction of stabilizer in DySZPB.

For the additional secondary phase addition in the DySZPB coating, it was expected that the BN with a hexagonal, graphitic structure would act as a dislocating agent. This dislocating agent promotes abradability with the introduction of its weak bonding between basal planes. However, that expected behavior is challenged by the result in this study that the hexagonal structure is not maintained in the BN phase after APS processing. The amorphous form of BN present after processing nor its properties are known. Regardless, the lateral fracture dominated damage behavior in the DySZPB coatings with little extension through the coating thickness is more similar to the behavior seen in the damage zone of the bulk YSZ-hBN composite. This is seen in all the DySZPB coatings despite the increased hardness and extensive densification evident in microstructures with aging, which suggests this secondary phase plays a role in maintaining a constant damage accommodation mechanism.

A final significant finding shown in this work is that increased hardness does not always signify a decrease in abradability, which is the current understanding in literature to date. The DySZPB coatings showed the most extensive densification and a larger than two fold increase in hardness with aging yet maintained a constant behavior with little damage accommodation extending deep within the material. The extent of densification in YSZP, however, does not cause a significant increase in hardness of the aged coatings. Yet, the damage accommodation behavior of the YSZP coatings changes at higher aging times. This signifies that hardness alone is not a good predictor of the ease of abradability because it is unable to give insight into the underlying damage accommodation mechanism for materials with a range of microstructural features.

In the YSZP coatings, the additional presence of nanozone features, shown in literature to enhance abradability under certain conditions or even introduce plastic-like behavior to the coating, do not show the expected damage accommodation mechanism [45]. The as processed and YSZP coating aged for 50 hours show a large damage zone beneath the macroscratch track that extends deep within the coating. It is characteristic of a brittle fracture in the coating with a microcrack network penetrating the weak intercolumnar grains within a splat, thereby breaking up the APS splat features. A similar behavior of crack formation and propagation into the material is seen in the dense, bulk 4YSZ macroscratch damage zone. The highly intergranular fracture seen in the t' 4YSZ bulk material is attributed to the use of the SPS process and fast cooling rate, which produced high residual stress in the coating making it unsuitable for comparison. However, with 145 hours of exposure at 1100˚C and 9.5% H_2O (v), the damage behavior in the YSZP changes to a more lateral fracture with little damage seen beneath the scratch track. Literature studies on APS YSZ have shown that aging increases the modulus and fracture toughness as well as reduces the amount of APS defects present in the coating [58]. From studies on the wear of ceramics, it is known that the extent of lateral and radial cracking is mainly controlled by hardness and fracture toughness with low hardness and fracture toughness resulting in more radial and lateral cracking [59,60]. It is expected that the extent of densification in the YSZP coating aged for 145 hours was sufficient to increase the coating modulus and fracture toughness, which changed the observed damage behavior.

A final significant finding shown in this work is that increased hardness does not always signify a decrease in abradability, which is the current understanding in literature to date. The DySZPB coatings showed the most extensive densification and a larger than two fold increase in hardness with aging yet maintained a constant behavior with little damage accommodation extending deep within the material. The extent of densification in YSZP, however, does not cause a significant increase in hardness of the aged coatings. Yet, the damage accommodation behavior of the YSZP coatings changes at higher aging times. This signifies that hardness alone is not a good predictor of the ease of abradability because it is unable to give insight into the underlying damage accommodation mechanism for materials with a range of microstructural features.

5. Summary

Abradable coatings are used for clearance control in both aerospace and power generation turbines to improve gas flow utilization for producing mechanical energy. The use of abradable coatings in turbine hot sections requires the implementation of ceramic materials, which are inherently brittle, creating a unique combination of properties that must be met in the design of these coating systems. Until this study, that unique combination of properties was only known to the extent that a certain set of processing parameters were connected to enhanced performance when tested with mostly industrial-scale test rigs. The findings of this study give insight into the different mechanisms by which ceramic abradable coatings can accommodate damage, the key microstructural features that enable these accommodation mechanisms, and the evolution of behavior in the coatings under simulated working conditions. These insights can be used to guide design strategies for the next generation of ceramic abradable coatings that are able to withstand more harsh environments and higher temperatures. The design of current technology ceramic abradable

coatings utilizes air plasma spray processing (APS) with tetragonal yttria stabilized zirconia (YSZ), or variants thereof, as the matrix material. Additional APS processing modifications or material modifications have been made to increase the abradability of YSZ; the strategies are discussed below and illustrated in **Figure 41** as compared to that of typical APS microstructures.

Key insights into the effect of microstructural design in promoting desirable abradable behavior have been shown in this study through the use of a lab-scale macroscratch test. DySZPB coatings show a significant increase in hardness with aging due to a high extent of densification resulting in the removal of open splat boundaries. This increase in hardness was thought previously to degrade abradable performance. However, these coatings show predictable damage behavior with aging and little to no damage extension to the microstructure beneath the scratch track, which is attributed to the presence of the secondary BN phase. The YSZP coatings, on the other hand exhibit highly brittle fracture changing only with longer aging times. Since interactions with the blade are expected upon first startup of the engine as well as with higher operating times, this brittle fracture could not only compromise the integrity of the remaining coating but also send debris to impact turbine components further downstream. Further work must be done to understand the significance of secondary phase additions in abradable coating behavior, as well as how these lab-scale tests compare to testing at higher strain rates and temperatures.

.

LIST OF TABLES

LIST OF FIGURES

Figure 11: Schematic showing the setup of the high temperature, controlled atmosphere tube furnace used for aging experiments.

Figure 12: Representative coupons of the five material compositions prepared by Air Plasma Spray (APS) deposition.

Figure 13: Image of two abradable material compositions prepared by air plasma spray at Solar Turbines Incorporated. Free standing coatings were obtained of Metco 2460NS (YSZ, polyester – left) and Durabrade 2192 (DySZ, polyester, BN – right) abradable systems.

Figure 14: SEM images of bulk t YSZ, t' YSZ, and t YSZ-hBN materials.

Figure 15: XRD of YSZ-hBN bulk material showing the presence of t 4YSZ, hBN, and an additional oxidized zirconium boride phase.

Figure 16: XRD showing an inset from two theta: 72-74 degrees confirming the presence of the metastable t' phase in the SPS processed bulk YSZ.

Figure 17: SEM images of the as processed coating materials with coatings processed by PlasmaTech. shown on top and Solar Turbines on the bottom.

Figure 18: SEM image showing the presence of nanozone features in the YSZP_ST coating.

Figure 19: Raman spectrum representative of the as processed DySZPB coating (aged for 50 hrs. shown for example) as compared to the as received DySZPB powders.

Figure 20: TEM image of the amorphous area of BN found in the DySZPB coatings.

Figure 21: SEM images showing the progression of the microstructures of the DySZPB coatings with aging.

Figure 22: SEM images showing the progression of the microstructures of the YSZP_ST coatings with aging at 145 hours.

Figure 23: SEM of YSZP and DySZPB coatings exposed at 9.5% water vapor for 145 hrs. showing the further extent of sintering seen in the DySZPB coatings at higher magnification.

Figure 24: Fracture surface SEM images of as processed and aged DySZPB (70 hrs. shown).

Figure 25: Vicker's hardness compared for the bulk t YSZ, t' YSZ, and YSZ-hBN composite.

Figure 26: Vicker's hardness of as processed and aged coatings as compared to a standard 4YSZ APS TBC.

Figure 27: SEM images of the as received APS coatings scratched with the nanoindenter.

Figure 28: SEM image of the nanoindenter scratch track of the as processed YSZP_ST1q showing surface and radial cracking.

Figure 29: SEM image and measurements of the scratch track by optical vibrometer showing the as processed nanoindenter scratched DySZPB coating.

Figure 30: 3D optical vibrometer image of the YSZP_ST coating aged for 145 hrs at 30% H_2O (v) showing material pileup along the edges of the scratch track made by progressive loading with the nanoindenter tip.

Figure 31: Raw data from the nanoindenter scratch test showing inconsistent measurements of the APS coatings.

Figure 32: SEM image of the as processed YSZP_ST coating showing a high tortuous scratch track.

Figure 33: Cross sectional SEM images showing the damage zones of the bulk materials post macroscratch testing.

Figure 34: SEM image of the t and t' YSZ macroscratch tracks showing the highly transgranular fracture seen in the SPS processed t' YSZ.

Figure 35: Optical vibrometer topography image and line scans for macroscratched bulk YSZ, taken with vibrometer preset surface parameter 'smooth with step'.

Figure 36: Optical vibrometer topography image and line scans for macroscratched bulk YSZ-hBN, taken with vibrometer preset surface parameter 'rough' due to the rougher surface in the composite from pullout during polishing.

Figure 37: Optical vibrometer topography image and line scans for macroscratched YSZP.

Figure 38: Optical vibrometer topography image and line scans for macroscratched DySZPB.

Figure 39: Cross sectional SEM images showing the damage zone evolution for macroscratched YSZP_ST and DySZPB coatings with aging.

Figure 40: Higher magnification cross sectional SEM images showing the different damage zone characteristics in the YSZP_ST (aged, 50 hrs. shown for example) versus DySZPB (as processed shown).

Figure 41: Schematic showing different design strategies for enabling abradability in ceramic APS coatings. Image A shows typical APS microstructural features, while images B and D show process modifications, such as dense vertical cracked microstructures (B) or pillars deposited on the coating surface (D). Images C1, C2, and E show material modifications. C1 and C2 show nanozone features and coarse porosity while E shows secondary phase additions.

REFERENCES

[1] A. G. Evans, D. R. Mumm, J. W. Hutchinson, G. H. Meier, and F. S. Pettit, "Mechanisms Controlling the Durability of Thermal Barrier Coatings," *Prog. Mater. Sci.,* **46** [5] 505-53 (2001).

[2] R. W. Ames, B. M. White and P. Burke, "Conditions in Advanced Turbines For IGCC Power Plants with Carbon Capture," *Proceedings of the ASME Turbo Expo 2013 TE2013* (2013).

[3] D. M. Lipkin, J. A. Krogstad, Y. Gao, C. A. Johnson, W. A. Nelson, and C. G. Levi, "Phase Evolution upon Aging of Air-Plasma Sprayed t'-Zirconia Coatings: I – Synchrotron X-Ray Diffraction," *J. Am.Ceram. Soc.,* **96** [1] 290-98 (2013).

[4] J. A. Krogstad, R. M. Leckie, S. Kramer, J. M. Cairney, D. M. Lipkin, C. A. Johnson, and C. G. Levi, "Phase Evolution upon Aging of Air Plasma Sprayed t'-Zirconia Coatings: II – Microstructure Evolution," *J. Am.Ceram. Soc.,* **96** [1] 299-307 (2013).

[5] A. M. Limarga, J. Iveland, M. Gentleman, D. M. Lipkin, and D. R. Clarke, "The Use of Larson-Miller Parameters to Monitor the Evolution of Raman Lines of Tetragonal Zirconia with High Temperature Aging," *Acta Mater.,* **59** [3] 1162-67 (2011).

[6] G. Di Girolamo, C. Blasi, L. Pagnotta, and M. Schioppa, "Phase Evolution and Thermophysical Properties of Plasma Sprayed Thick Zirconia Coatings after Annealing," *Ceram. Int.,* **36** [8] 2273-80 (2010).

[7] J. A. Krogstad, S. Kramer, D. M. Lipkin, C. A. Johnson, D. R. G. Mitchell, J. M. Cairney, and C. G. Levi, "Phase Stability of t'-Zirconia-Based Thermal Barrier Coatings: Mechanistic Insights," *J. Am.Ceram. Soc.,* **94** s168-77 (2011).

[8] K. Kobayashi, H. Kuwajima, and T. Masaki, "Phase Change and Mechanical Properties of ZrO_2-Y_2O_3 Solid Electrolyte After Aging," *Solid State Ion.,* **3-4**, 489-93 (1981).

[9] J. Chevalier, B. Cales, and J. M. Drouin, "Low-Temperature Aging of Y-TZP Ceramics," *J. Am.Ceram. Soc.,* **82** [8] 2150-54 (1999).

[10] T. Sato and M. Shimada, "Transformation of Yttria-Doped Tetragonal ZrO_2 Polycrystals by Annealing in Water," *J. Am.Ceram. Soc.,* **68** [6] 356-59 (1985).

[11] F. F. Lange, G. L. Dunlop, and B. I. Davis, "Degradation During Aging of Transformation-Toughened ZrO_2-Y_2O_3 Materials At 250°C," *J. Am.Ceram. Soc.,* **69** [3] 237-40 (1986).

[12] M. Yoshimura, T. Noma, K. Kawabata, and S. Somiya, "Role of H_2O on the Degradation Process of Y-TZP," *J. Mater. Sci. Lett.,* **6** [4] 465-67 (1987).

[13] D. J. Kim, H. J. Jung, and D. H. Cho, "Phase-Transformations of Y_2O_3 And Nb_2O_5 Doped Tetragonal Zirconia During Low-Temperature Aging in Air," *Solid State Ion.,* **80** [1-2] 67-73 (1995).

[14] A. E. Hughes, F. T. Ciacchi, and S. P. S. Badwal, "Role of O^{2-}, OH^- and Anion Vacancies in the Degradation of Y-TZP in Moist Environments," *J. Mater. Chem.,* **4** [2] 257-63 (1994).

[15] J. Chevalier, L. Gremillard, A. V. Virkar, and D. R. Clarke, "The Tetragonal-Monoclinic Transformation in Zirconia: Lessons Learned and Future Trends," *J. Am.Ceram. Soc.,* **92** [9] 1901-20 (2009).

[16] J. A. Dawson and I. Tanaka, "Proton incorporation and trapping in ZrO_2 grain boundaries," *J. Mater. Chem. A*, **2** [5] 1400-08 (2014).

[17] J. A. Dawson, H. R. Chen, and I. Tanaka, "Protonic defects in yttria stabilized zirconia: incorporation, trapping and migration," *Phys. Chem. Chem. Phys.*, **16** [10] 4814-22 (2014).

[18] T. Duong, A. M. Limarga, and D. R. Clarke, "Diffusion of Water Species in Yttria-Stabilized Zirconia," *J. Am.Ceram. Soc.,* **92** [11] 2731-37 (2009).

[19] B. Scherrer, M. V. F. Schlupp, D. Stender, J. Martynczuk, J. G. Grolig, H. Ma, P. Kocher, T. Lippert, M. Prestat, and L. J. Gauckler, "On Proton Conductivity in Porous and Dense Yttria Stabilized Zirconia at Low Temperature," *Adv. Funct. Mater.*, **23** [15] 1957-64 (2013).

[20] J. S. Park, Y. B. Kim, J. H. Shim, S. Kang, T. M. Gur, and F. B. Prinz, "Evidence of Proton Transport in Atomic Layer Deposited Yttria-Stabilized Zirconia Films," *Chem. Mat.*, **22** [18] 5366-70 (2010).

[21] B.H. Toby, "EXPGUI, a graphical user interface for GSAS," *J. Appl. Crystallogr.,* **34** [4] 210-13 (2001).

[22] G. Teufer, "Crystal Structure of Tetragonal ZrO^2," *Acta Crystallogr.,* **15,** 1187-& (1962).

[23] C. J. Howard, R. J. Hill, and B. E. Reichert, "Structures of the ZrO_2 Polymorphs at Room-Temperature by High-Resolution Neutron Powder Diffraction," *Acta Crystallogr. Sect. B: Struct. Sci.,* **44,** 116-20 (1988).

[24] P. Thompson, D. E. Cox, and J. B. Hastings, "Rietveld Refinement of Debye-Scherrer Synchrotron X-Ray Data from Al_2O_3," *J. Appl. Crystallogr.,* **20,** 79-83 (1987).

[25] C. J. Howard and R. J. Hill, "The Polymorphs of Zirconia - Phase Abundance and Crystal-Structure by Rietveld Analysis of Neutrona X-Ray-Diffraction Data," *J. Mater. Sci.,* **26** [1] 127-34 (1991).

[26] L. B. McCusker, R. B. Von Dreele, D. E. Cox, D. Louer, and P. Scardi, "Rietveld Refinement Guidelines," *J. Appl. Crystallogr.,* **32,** 36-50 (1999).

[27] J. F. Jue, J. Chen, and A. V. Virkar, "Low-Temperature Aging of t'-Zirconia - The Role of Microstructure on Phase-Stability," *J. Am.Ceram. Soc.,* **74** [8] 1811-20 (1991).

[28] T. Sakuma, Y.I. Yoshizawa, and H. Suto, "The Modulated Structure Formed by Isothermal Aging in ZrO_2-5.2 mol% Y_2O_3 Alloy," *J. Mater. Sci.,* **20** [3] 1085-92 (1985).

[29] J. Ilavsky, J. K. Stalick, and J. Wallace, "Thermal Spray Yttria-Stabilized Zirconia Phase Changes During Annealing," *J. Therm. Spray Technol.,* **10** [3] 497-501 (2001).

[30] J. Ilavsky and J. K. Stalick, "Phase Composition and its Changes During Annealing of Plasma-Sprayed YSZ," *Surf. Coat. Technol.,* **127** [2-3] 120-29 (2000).

[31] A. H. Heuer and M. Ruhle, "On the Nucleation of the Martensitic-Transformation in Zirconia (ZrO_2)," *Acta Metall.,* **33** [12] 2101-12 (1985).

[32] S. E. Redfern, R. W. Grimes, and R. D. Rawlings, "The Hydroxylation of t-ZrO_2 Surfaces," *J. Mater. Chem.,* **11** [2] 449-55 (2001).

[33] S. P. S. Badwal and N. Nardella, "Formation of Monoclinic Zirconia at the Anodic Face of Tetragonal Zirconia Polycrystalline Solid Electrolytes," *Appl. Phys. A-Mater. Sci. Process.,* **49** [1] 13-24 (1989).

[34] D. J. Kim, J. W. Jang, and H. L. Lee, "Effect of Tetravalent Dopants on Raman Spectra of Tetragonal Zirconia," *J. Am.Ceram. Soc.,* **80** [6] 1453-61 (1997).

[35] D. J. Kim, H. J. Jung, and I. S. Yang, "Raman-Spectroscopy of Tetragonal Zirconia Solid-Solutions," *J. Am.Ceram. Soc.,* **76** [8] 2106-08 (1993).

[36] R. Chaim, A. H. Heuer, and D. G. Brandon, "Phase Equilibration in ZrO_2-Y_2O_3 Alloys by Liquid-Film Migration," *J. Am.Ceram. Soc.,* **69** [3] 243-48 (1986).

[37] E. J. Opila, D. S. Fox, and N. S. Jacobson, "Mass Spectrometric Identification of Si-O-H(g) Species

from the Reaction of Silica with Water Vapor at Atmospheric Pressure," *J. Am.Ceram. Soc.,* **80** [4] 1009-12 (1997).

[38] H. Schubert and F. Frey, "Stability of Y-TZP During Hydrothermal Treatment: Neutron Experiments and Stability Considerations," *J. Eur. Ceram. Soc.*, **25** [9] 1597–602 (2005).

[39] B. Kiho, S. Kyung Sik, K. Jun Woo, P. Suk Won, A. Jihwan, F.B. Prinz, S. Joon Hyung, "Proton incorporation in yttria-stabilized zirconia during atomic layer deposition," *Int. J. Hydrog. Energy*, **39** [6] 2621-2627 (2014).

[40] M. Yashima, M. Kakihana, and M. Yoshimura, "Metastable-stable phase diagrams in the zirconia-containing systems utilized in solid-oxide fuel cell application," *Solid State Ion.*, **86-8** 1131-1149 (1996).

[41] F. R. Chien and A. H. Heuer, "Lattice diffusion kinetics in Y_2O_3-stabilized cubic ZrO_2 single crystals: A dislocation loop annealing study," *Philos. Mag. A*, **73-3** 681-697 (1996).

[42] Xu, Z. *et al.* Large-scale fabrication of porous YBO3 hollow microspheres with tunable photoluminescence. *R. Soc. OPEN Sci.* **5,** (2018).

[43] Knyrim, J. S. & Huppertz, H. High-pressure synthesis, crystal structure, and properties of the first ternary zirconium borate beta-ZrB2O5. *Z. NATURFORSCHUNG Sect. B- J. Chem. Sci.* **63,** 707–712 (2008).

[44] Aussavy, D. *et al.* YSZ-Polyester Abradable Coatings Manufactured by APS. *J. Therm. SPRAY Technol.* **25,** 252–263 (2016).

[45] Lima, R. S. & Marple, B. R. Thermal spray coatings engineered from nanostructured ceramic agglomerated powders for structural, thermal barrier and biomedical applications: A review. *J. Therm. SPRAY Technol.* **16,** 40–63 (2007).

[46] Saha, S. *et al.* Comparative high pressure Raman study of boron nitride nanotubes and hexagonal boron nitride. *Chem. Phys. Lett.* **421,** 86–90 (2006).

[47] Meschter, P. J., Opila, E. J. & Jacobson, N. S. Water Vapor-Mediated Volatilization of High-Temperature Materials. in *ANNUAL REVIEW OF MATERIALS RESEARCH, VOL 43* (ed. Clarke, DR) **43,** 559–588 (2013).

[48] Erk, K., Deschaseaux, C. & Trice, R. Grain-boundary grooving of plasma-sprayed yttria-stabilized zirconia thermal barrier coatings. *J. Am. Ceram. Soc.* **89,** 1673–1678 (2006).

[49] Cipitria, A., Golosnoy, I. O. & Clyne, T. W. A sintering model for plasma-sprayed zirconia TBCs. Part I: Free-standing coatings. *ACTA Mater.* **57,** 980–992 (2009).

[50] Strangman, T. Thermal Strain-Tolerant Abradable Thermal Barrier Coatings. *J. Eng. Gas Turbines Power-Trans. Asme* **114,** 264–267 (1992).

[51] Munawar, A. U., Schulz, U., Cerri, G. & Lau, H. Microstructure and cyclic lifetime of Gd and Dy-containing EB-PVD TBCs deposited as single and double-layer on various bond coats (vol 245C, pg 92, 2014). *Surf. Coat. Technol.* **279,** 53 (2015).

[52] Sporer, D. *et al.* Dysprosia stabilized zirconia abradable. (2007).

[53] Schaedler, T. A., Leckie, R. M., Kraemer, S., Evans, A. G. & Levi, C. G. Toughening of nontransformable t `-YSZ by addition of titania. *J. Am. Ceram. Soc.* **90,** 3896–3901 (2007).

[54] Tsipas, S. A. Effect of dopants on the phase stability of zirconia-based plasma sprayed thermal barrier coatings. *J. Eur. Ceram. Soc.* **30,** 61–72 (2010).

[55] Log, T., Cutler, R., Jue, J. & Virkar, A. Polycrystalline t'-$ZrO_2(Ln_2O_3)$ Formed By Displacive Transformations. *J. Mater. Sci.* **28,** 4503–4509 (1993).

[56] Anithakumari, P., Grover, V. & Tyagi, A. K. Structure-modulated ionic transport behavior in zirconia-dysprosia mixed oxides. *J. Mater. Sci.* **51,** 6711–6721 (2016).

[57] Hokkirigawa, K. Wear Mode Map Of Ceramics. *Wear* **151,** 219–228 (1991).

[58] Dwivedi, G., Viswanathan, V., Sampath, S., Shyam, A. & Lara-Curzio, E. Fracture Toughness of Plasma-Sprayed Thermal Barrier Ceramics: Influence of Processing, Microstructure, and Thermal Aging. *J. Am. Ceram. Soc.* **97,** 2736–2744 (2014).

[59] Kato, K. Tribology Of Ceramics. *Wear* **136,** 117–133 (1990).

[60] Evans, A. G. & Marshall, D. B. Wear Mechanisms In Ceramics. *Fundam. Frict. Wear Mater.* 439–451 (1981).

LIST OF ACRONYMS AND ABBREVIATIONS

HHC	High hydrogen content
YSZ	Yttria stabilizd zirconia
IGCC	Integrated gasification combined cycle
SEM	Scanning electron microscopy
EDS	Energy dispersive spectroscopy
BSE	Back-scattered electrons
XRD	X-ray Diffraction
STEM	Scanning transmission electron microscopy
GBRs	Grain boundary ridges
LMP	Larson Miller parameter
GIXRD	Grazing incedence X-ray diffraction
HTXRD	High temperature X-ray diffraction
TEC	Thermal expansion coefficient

TABLES

Table 1: Starting material specifications for Durabrade 2192 and Metco 2460NS powders.

Material	**Constituent Weight Percent (wt. %)**					**Powder Morphology; Particle Size**	**Operating Temp.**
Durabrade 2192	ZrO_2 balance	Dy_2O_3 9.5	hBN 0.7	Polyester 4.5	Impurities 0.1	Agglomerated; 176 +/- 11µm	1200˚C
Metco 2460NS	ZrO_2 balance	Y_2O_3 7.5	Binder 4	Polyester 4	Impurities 0.9	Agglomerated, HOSP, blended; 176 +/- 11µm	1200˚C

FIGURES

Figure 1: The $YO_{1.5}$–ZrO_2 phase diagram redrawn from Lipkin, *et al.* [3], showing the decomposition of the *t'* phase during isothermal aging at 1330°C. The metastable *t'* phase will decompose to the equilibrium tetragonal and cubic phases with increased aging times. The tetragonal phase will transform into the monoclinic phase upon cooling below the $T_0^{(t/m)}$ curve.

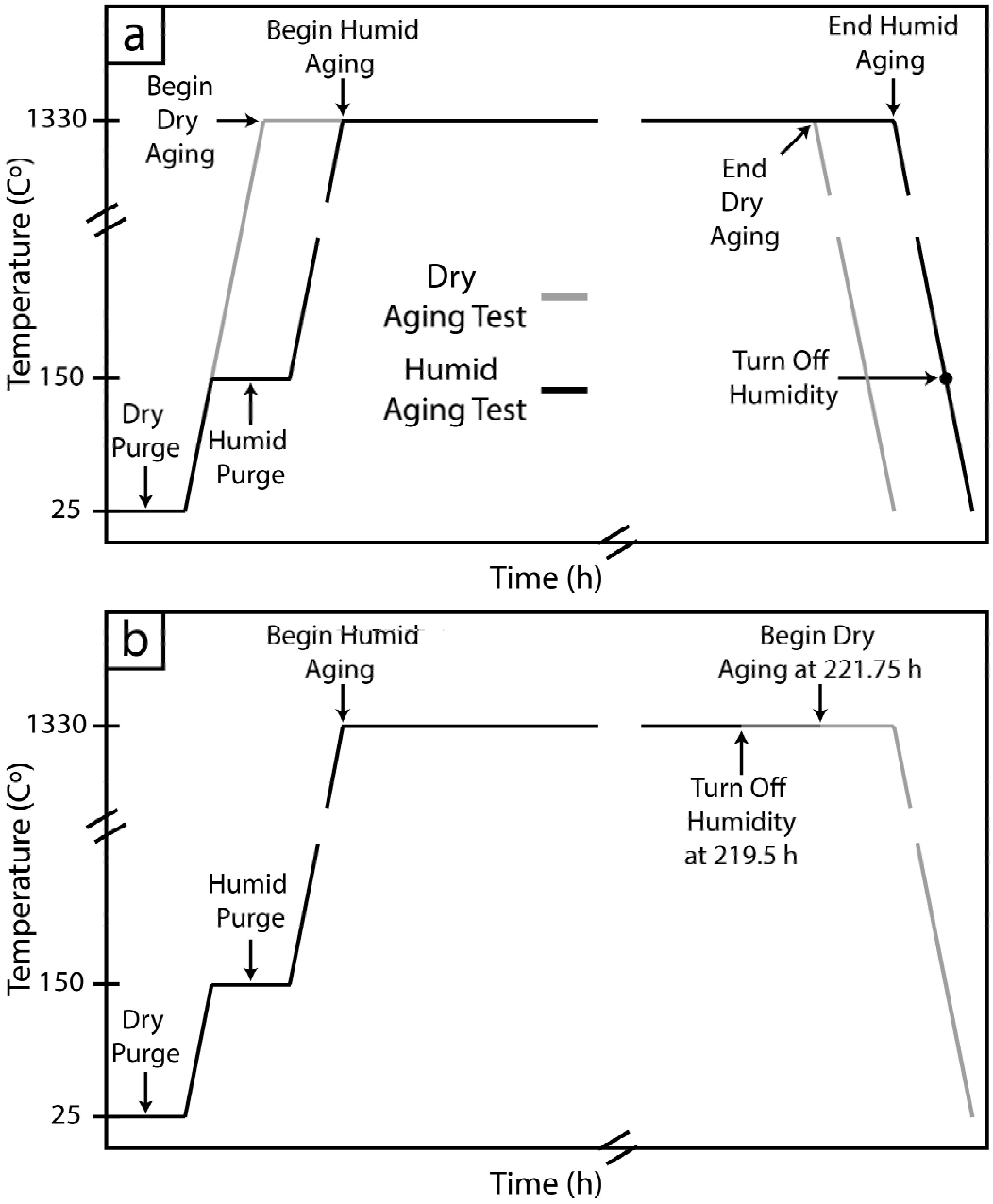

Figure 2: Examples of the heating protocols for the sample aging showing (a) the 140 h dry and humid tests and (b) the *hybrid 224 h* test.

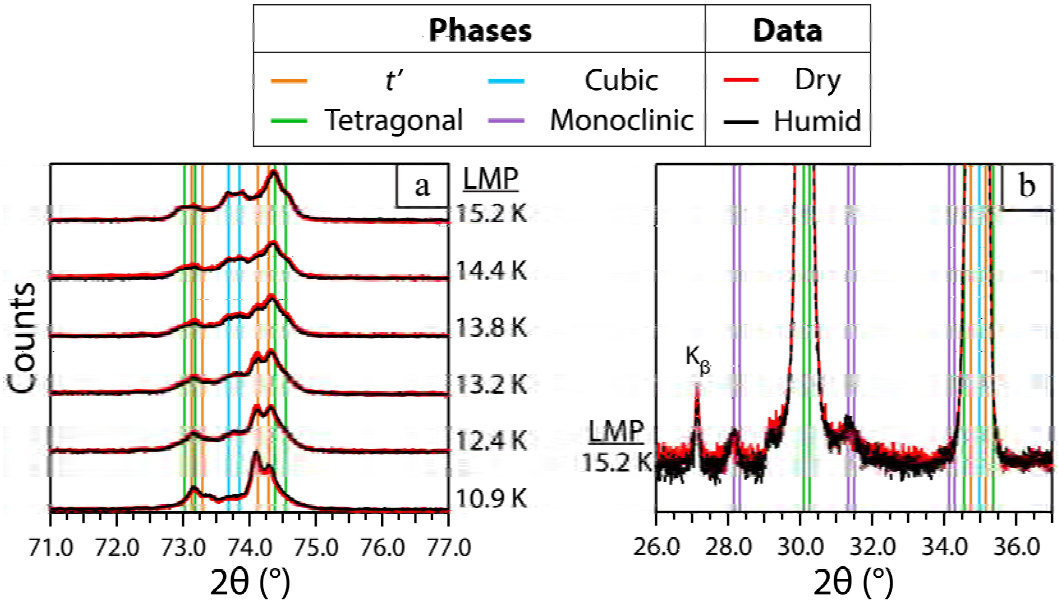

Figure 3: XRD spectra of the dry- and humid-aged APS 8YSZ for: (a) LMP 10.9 – 15.2 K (6 to 88 h) with the tetragonal planes (004) and (220) and the cubic plane (400), (b) LMP 15.2 K (88 h) showing the tetragonal planes (101), (002), and (110), the cubic planes (111) and (200), and the monoclinic planes ($11\bar{1}$), (111), (002)—the (101) and (111) lines overlap at this scale and are therefore indicated by one line. The angular positions as determined from the GSAS model are superimposed for the *t'*, tetragonal, cubic, and monoclinic phases. The $K\alpha_1/K\alpha_2$ doublet is shown by a pair of phase lines for each plane of atoms except when it overlaps with other phase lines.

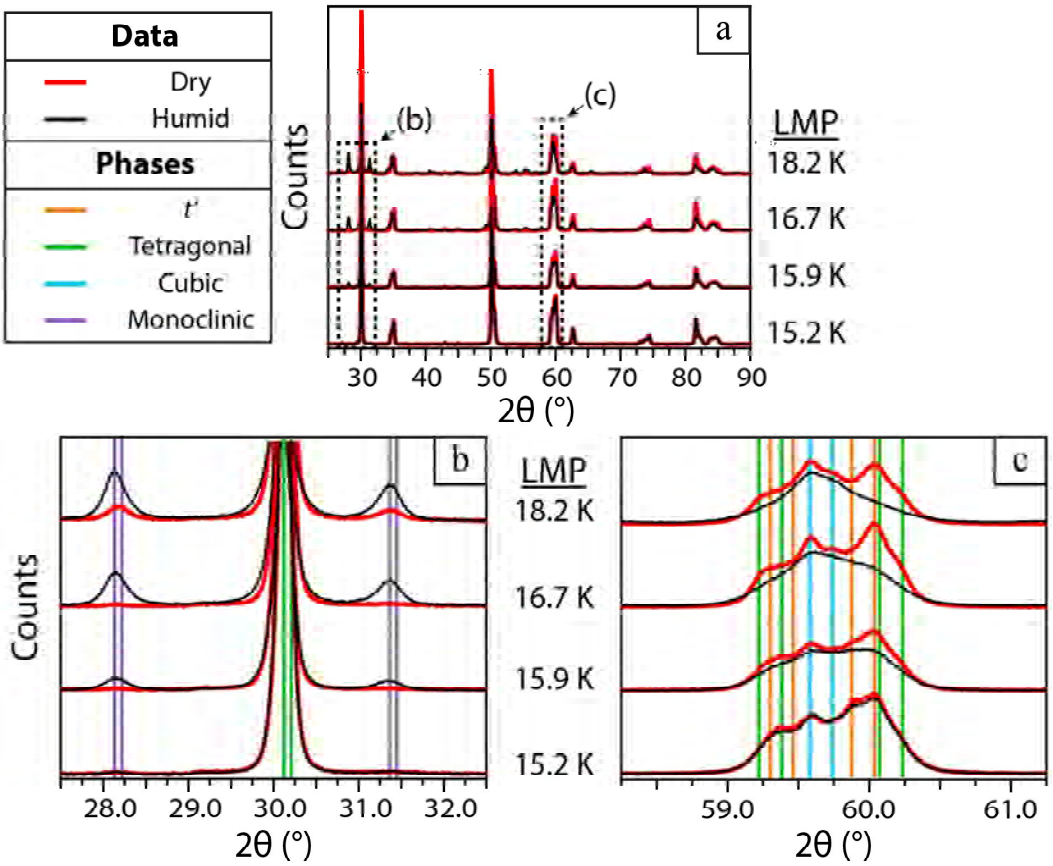

Figure 4: XRD spectra of the dry- and humid-aged APS 8YSZ from a LMP of 15.2 to 18.2 K (88 to 570 h) showing (a) the full spectrum, (b) the tetragonal plane (101), the cubic plane (111), and the monoclinic planes ($11\bar{1}$) and (111)— the (101) and (111) lines overlap at this scale and are therefore indicated by one line, and (c) the tetragonal planes (103) and (211) and the cubic plane (311). The angular positions as determined from the GSAS model are superimposed for the *t'*, tetragonal, cubic, and monoclinic phases. The $K\alpha_1/K\alpha_2$ doublet is shown by a pair of phase lines for each plane of atoms except when it overlaps with other phase lines.

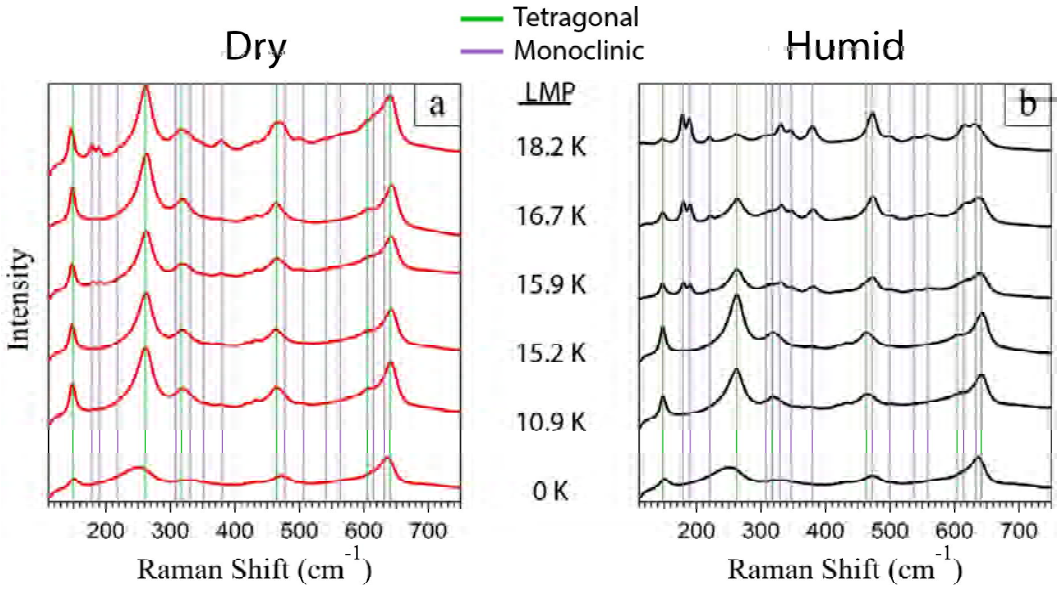

Figure 5: Raman spectra of the dry- and humid-aged APS 8YSZ samples. The locations of the characteristic tetragonal and monoclinic peaks are indicated by different lines.

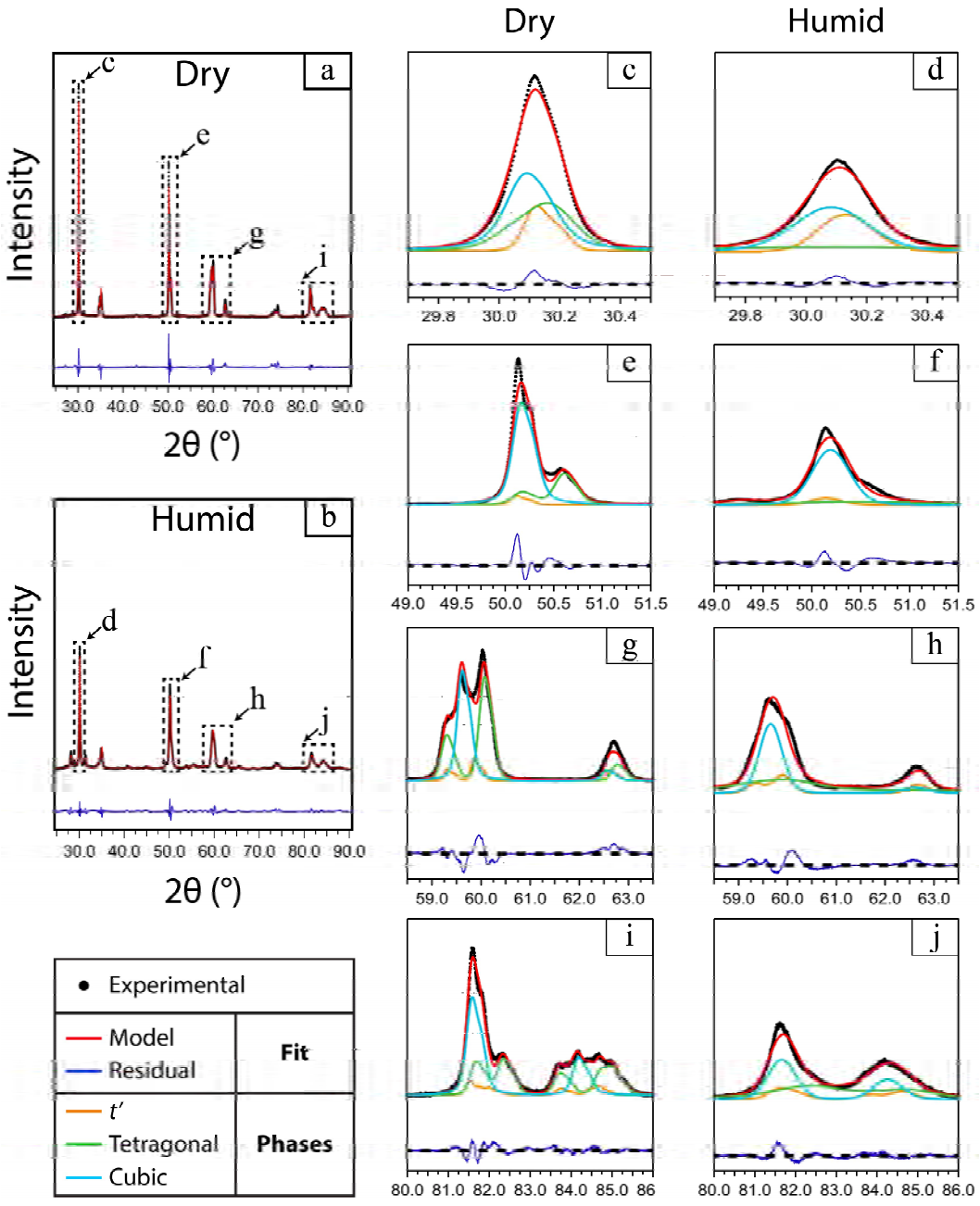

Figure 6: A comparison of the XRD spectra from the 16.7 K (224 h) dry- and humid-aged samples as well as the corresponding 4-phase model from GSAS.

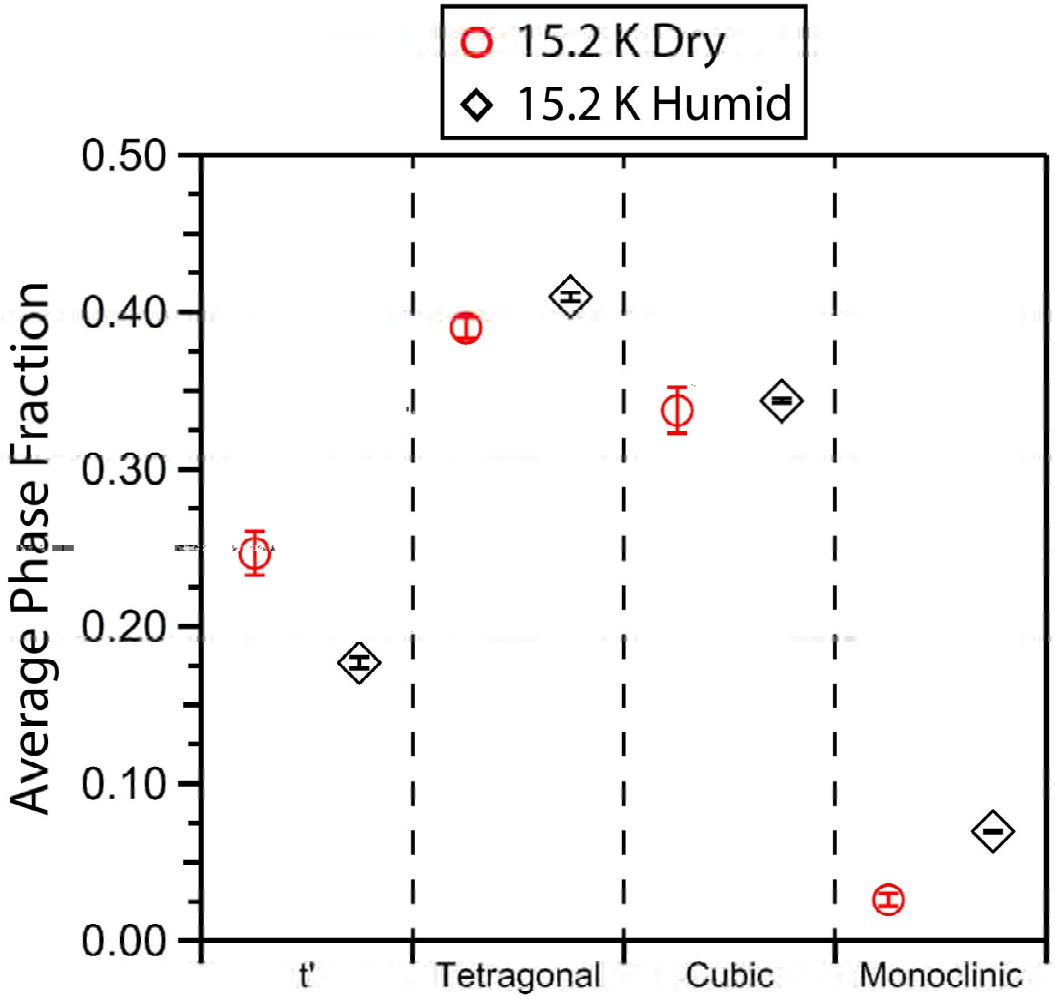

Figure 7: Average phase fraction values and standard deviations from the Rietveld analysis performed on the top, bottom, and polished-top of the 15.2 K (88 h) dry- and humid-aged 8YSZ samples. The phase fractions of the APS 8YSZ samples in the dry and humid environment were computed using the Rietveld method in GSAS.

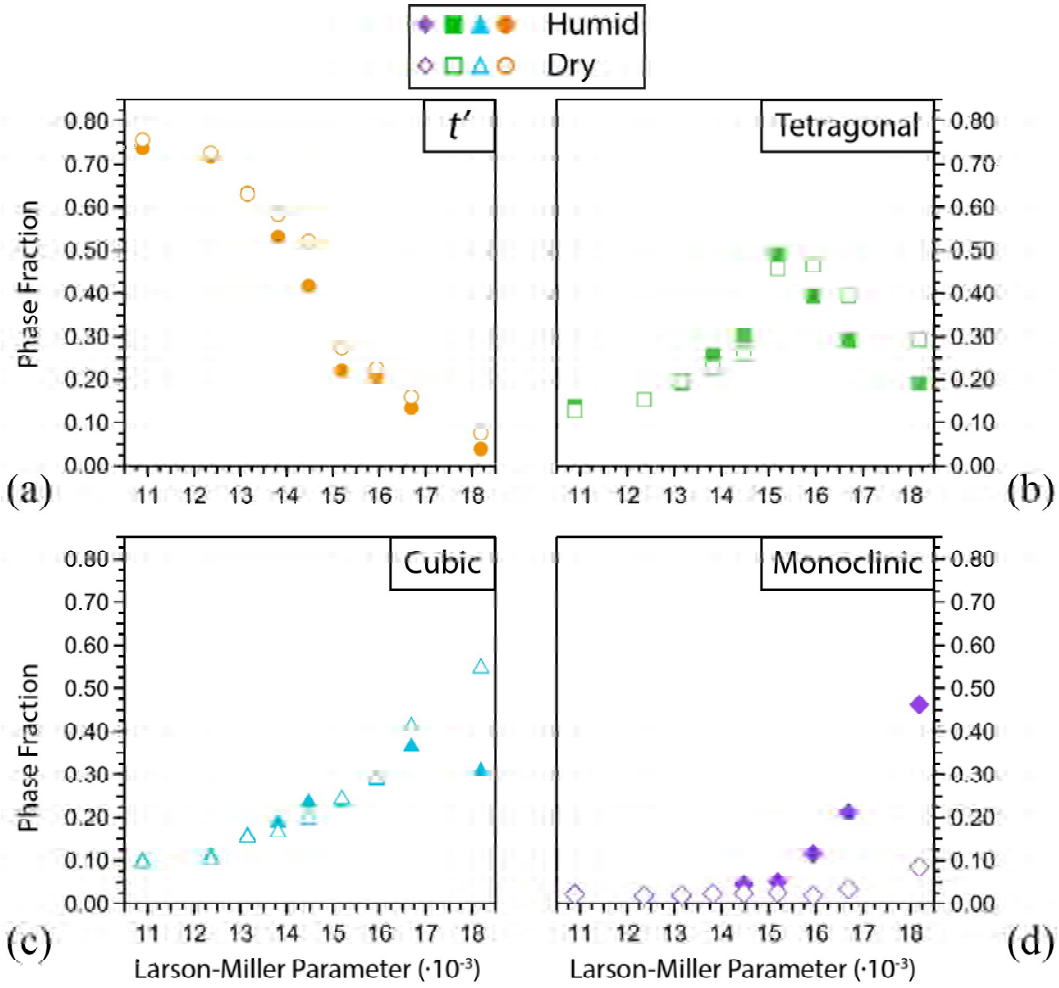

Figure 8: The phase fractions of the APS 8YSZ samples in the dry and humid environment computed using the Rietveld method in GSAS.

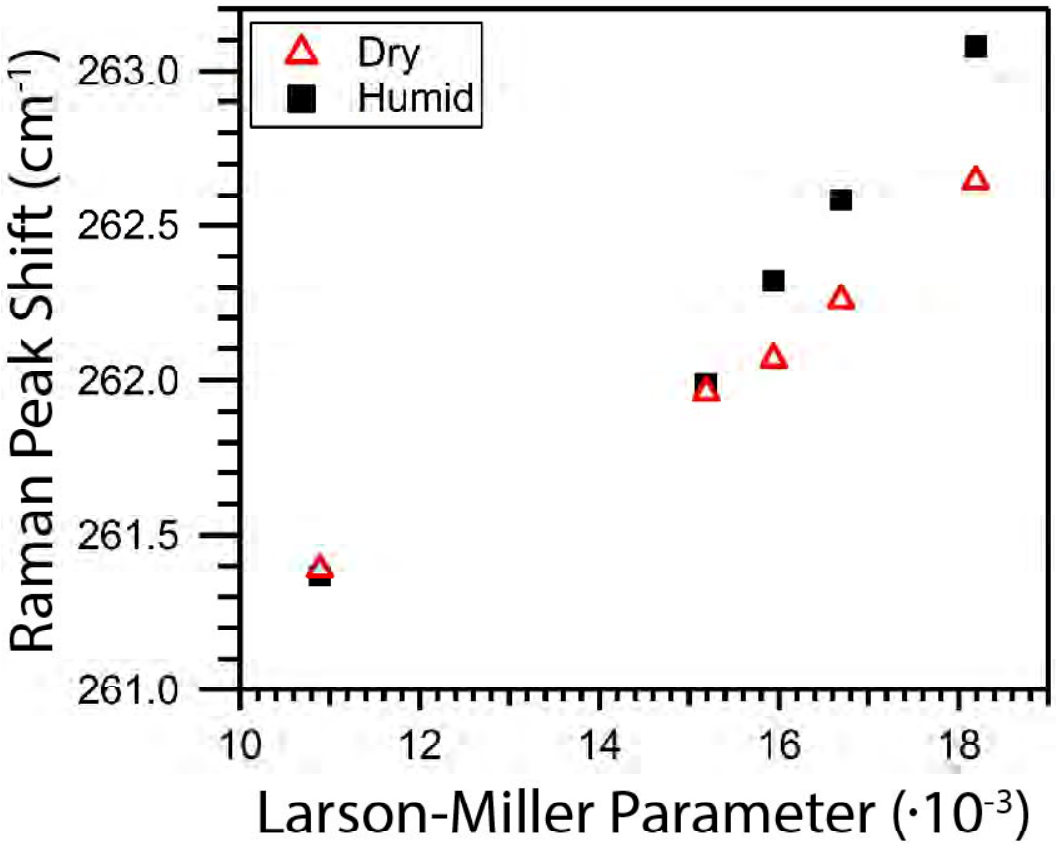

Figure 9: Peak fitting of the A_{1g} (259 cm^{-1}) mode of tetragonal zirconia for both the dry- and humid- aged environment.

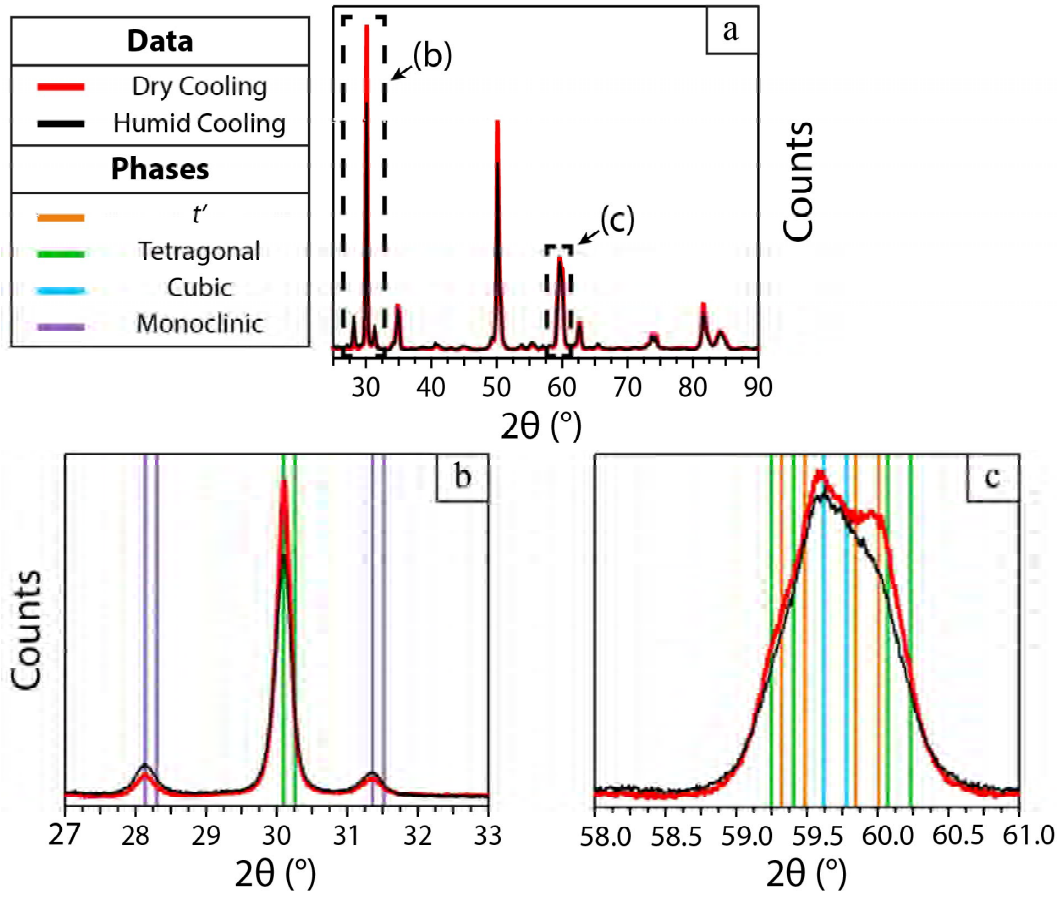

Figure 10: XRD spectra of the APS 8YSZ samples aged for 16.7 K (224 h) in a dry or humid cooling condition showing (a) the full spectrum, (b) the tetragonal plane (101), the cubic plane (111), and the monoclinic planes ($11\bar{1}$) and (111)—the (101) and (111) lines overlap at this scale and are therefore indicated by one line, and (c) the tetragonal planes (103) and (211) and the cubic plane (311). The angular positions as determined from the GSAS model are superimposed for the *t'*, tetragonal, cubic, and monoclinic phases. The $K\alpha_1/K\alpha_2$ doublet is shown by a pair of phase lines for each plane of atoms except when it overlaps with other phase lines.

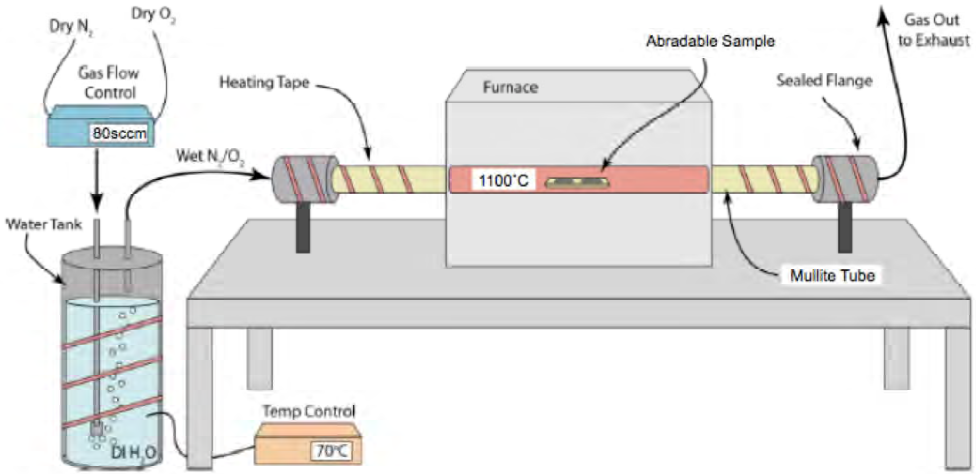

Figure 11: Schematic showing the setup of the high temperature, controlled atmosphere tube furnace used for aging experiments.

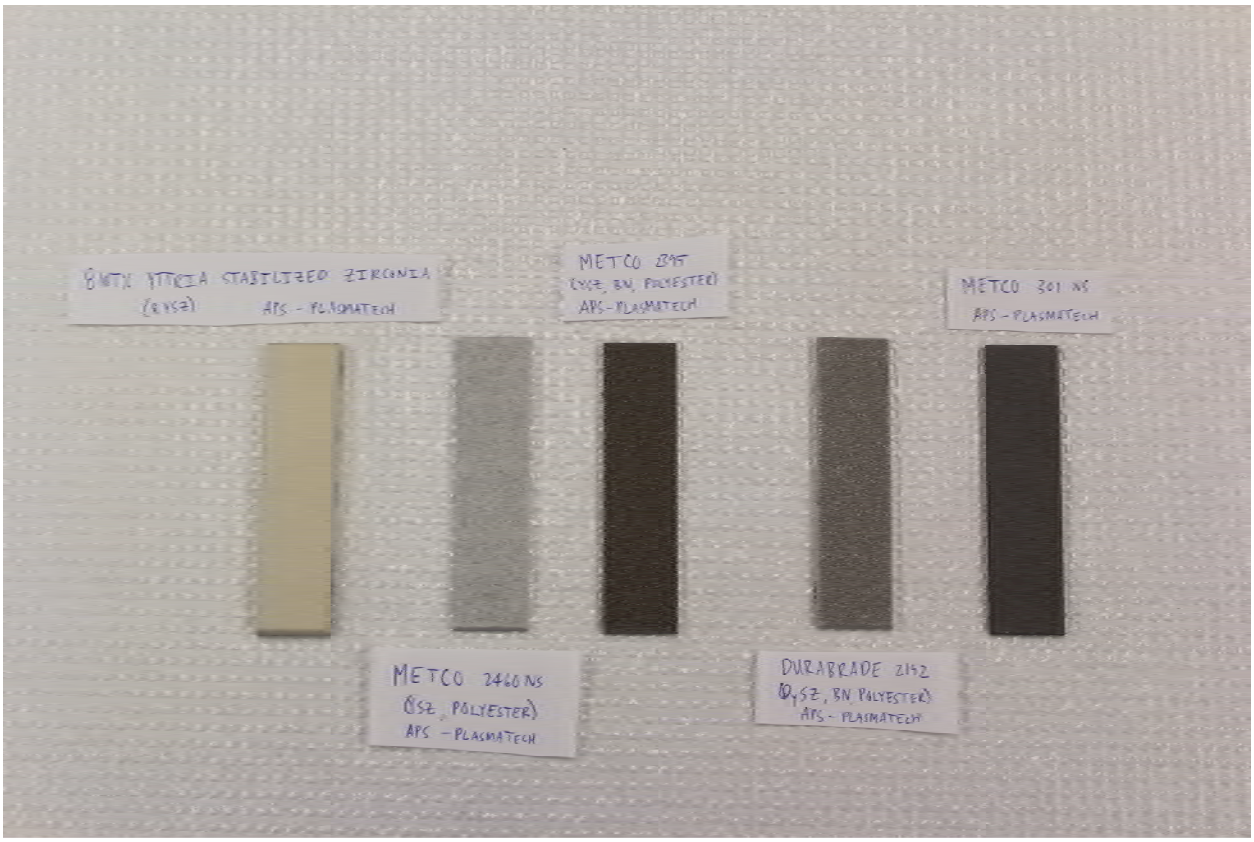

Figure 12: Representative coupons of the five material compositions prepared by Air Plasma Spray (APS) deposition.

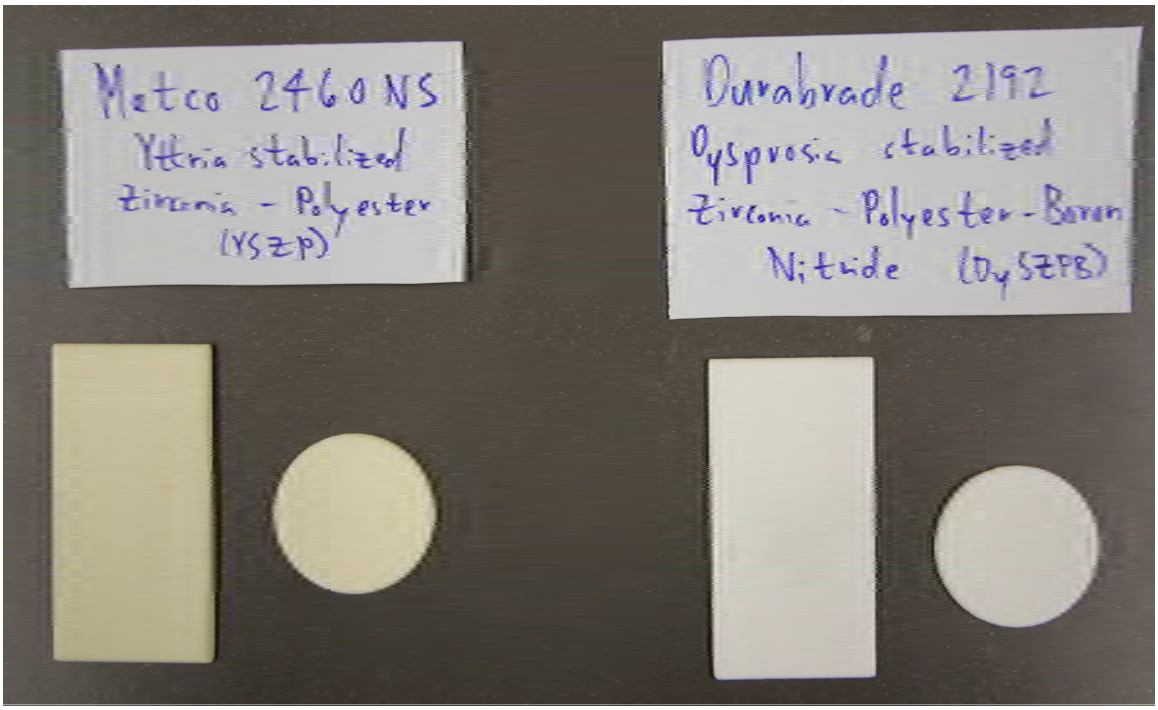

Figure 13: Image of two abradable material compositions prepared by air plasma spray at Solar Turbines Incorporated. Free standing coatings were obtained of Metco 2460NS (YSZ, polyester – left) and Durabrade 2192 (DySZ, polyester, BN – right) abradable systems.

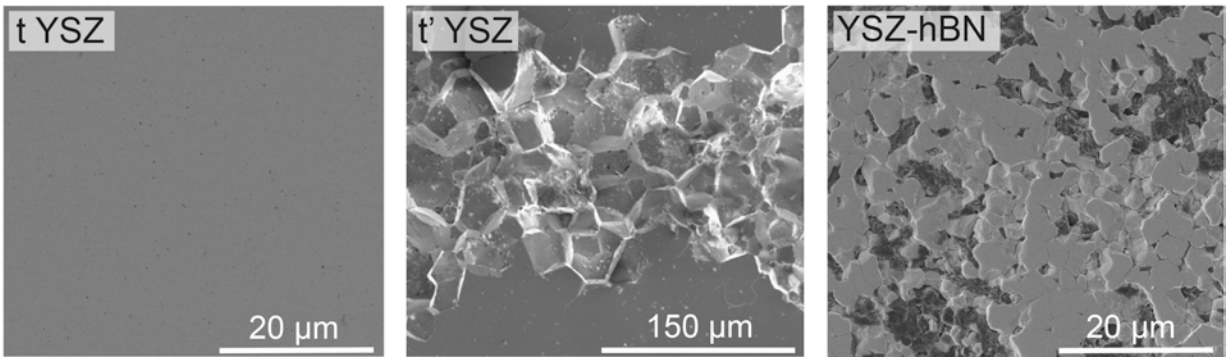

Figure 14: SEM images of bulk t YSZ, t' YSZ, and t YSZ-hBN materials.

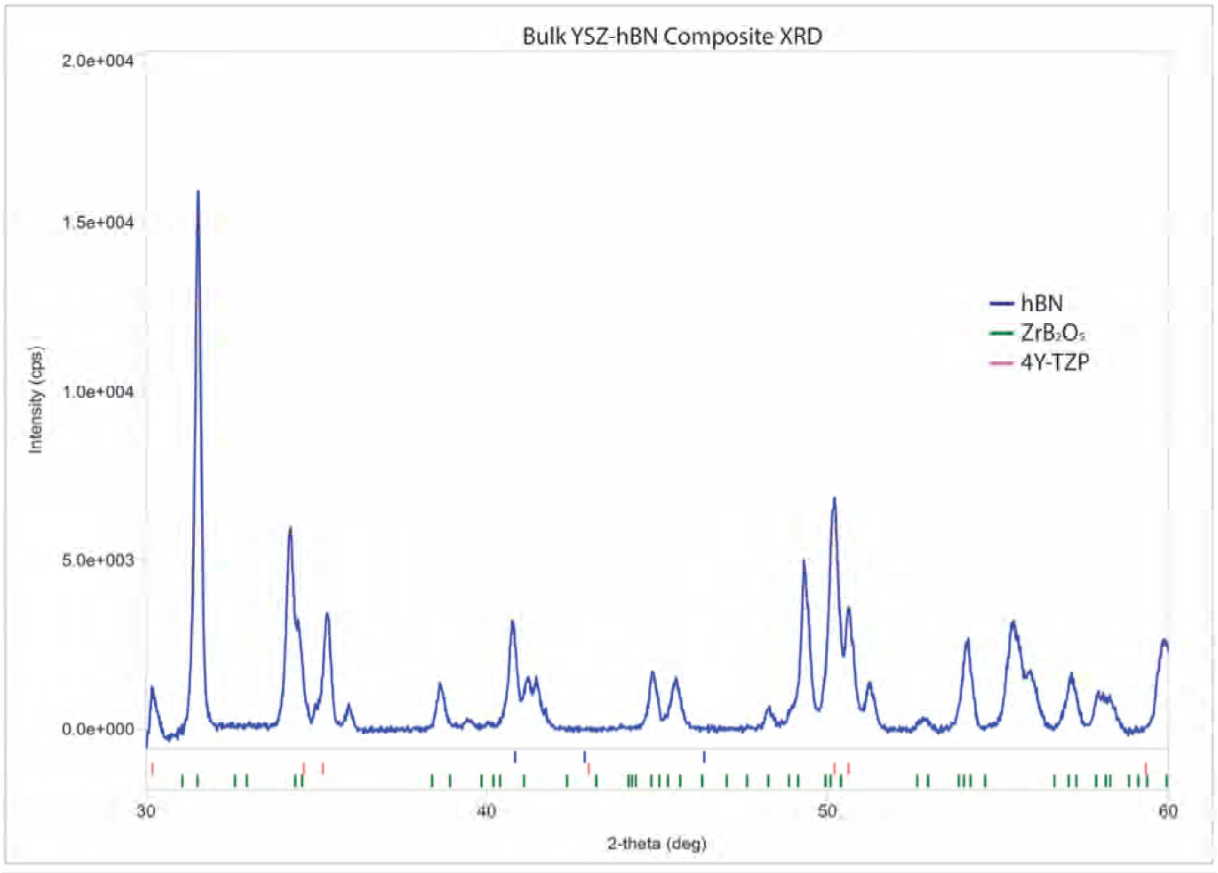

Figure 15: XRD of YSZ-hBN bulk material showing the presence of t 4YSZ, hBN, and an additional oxidized zirconium boride phase.

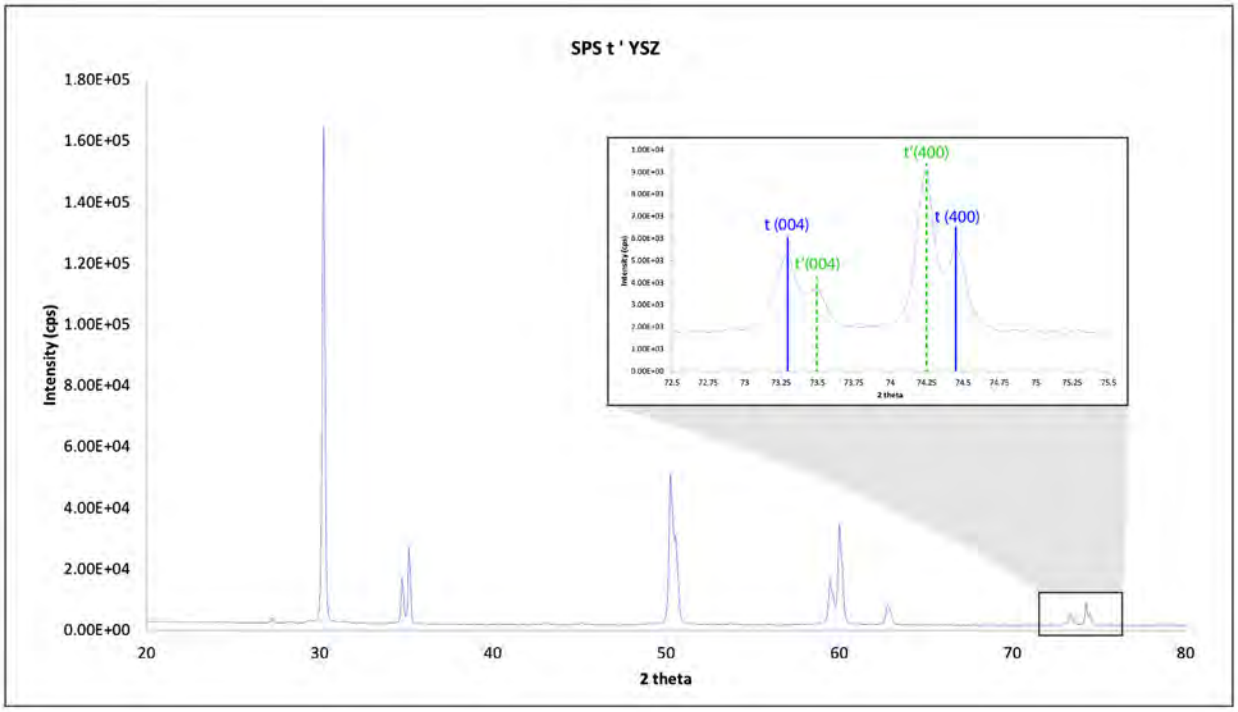

Figure 16: XRD showing an inset from two theta: 72-74 degrees confirming the presence of the metastable t' phase in the SPS processed bulk YSZ.

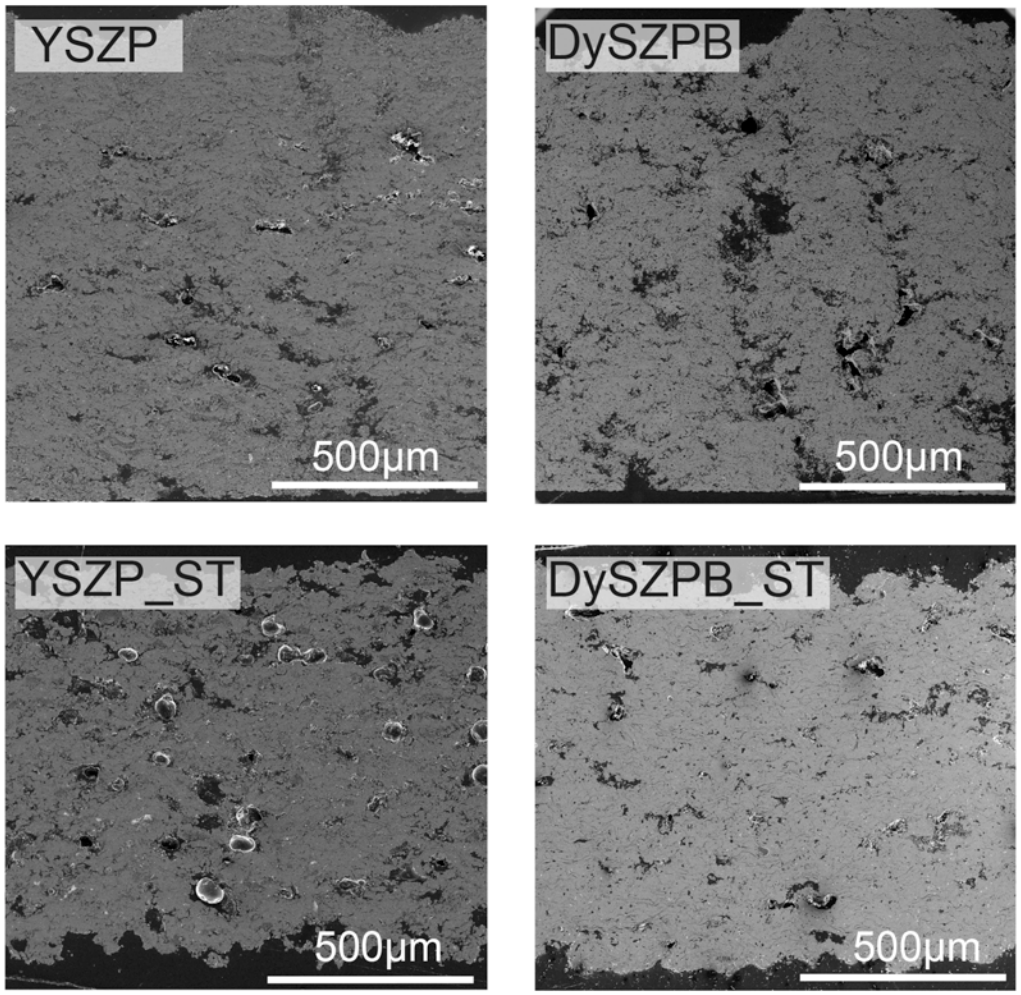

Figure 17: SEM images of the as processed coating materials with coatings processed by PlasmaTech. shown on top and Solar Turbines on the bottom.

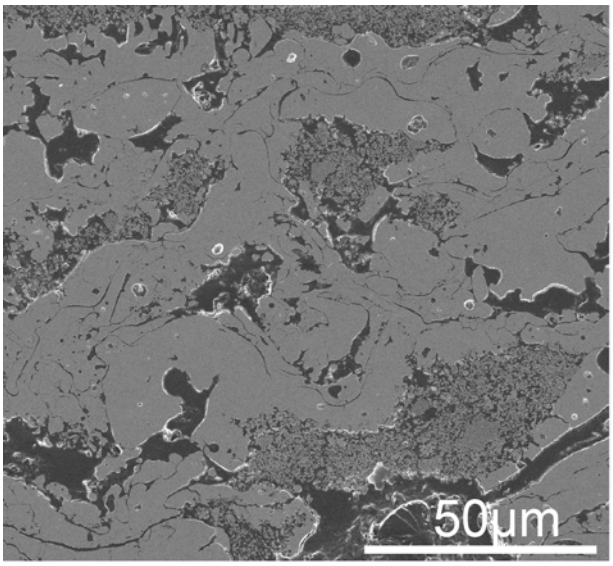

Figure 18: SEM image showing the presence of nanozone features in the YSZP_ST coating.

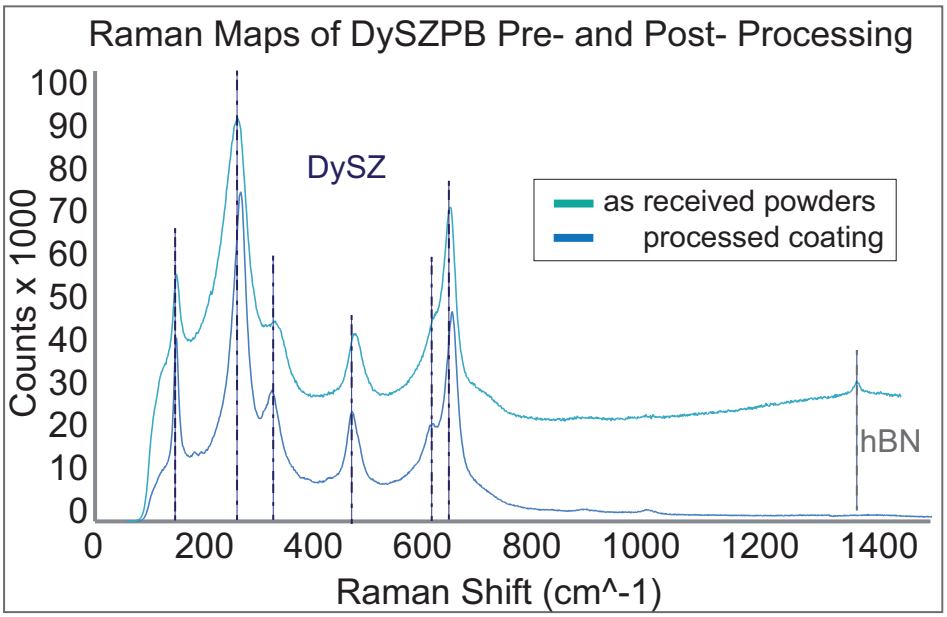

Figure 19: Raman spectrum representative of the as processed DySZPB coating (aged for 50 hrs. shown for example) as compared to the as received DySZPB powders.

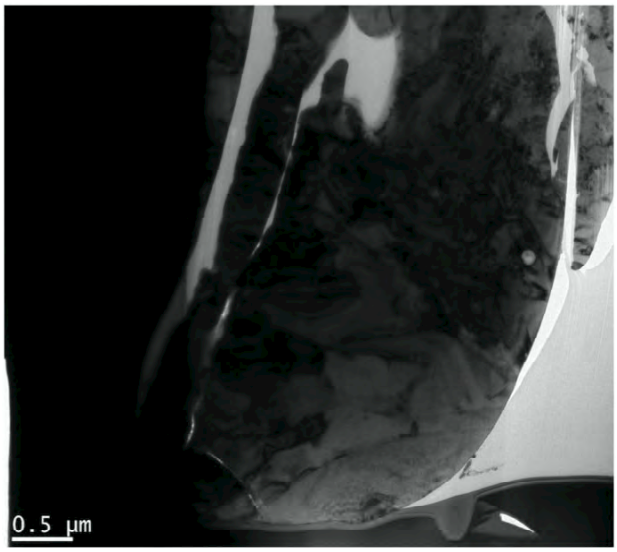

Figure 20: TEM image of the amorphous area of BN found in the DySZPB coatings.

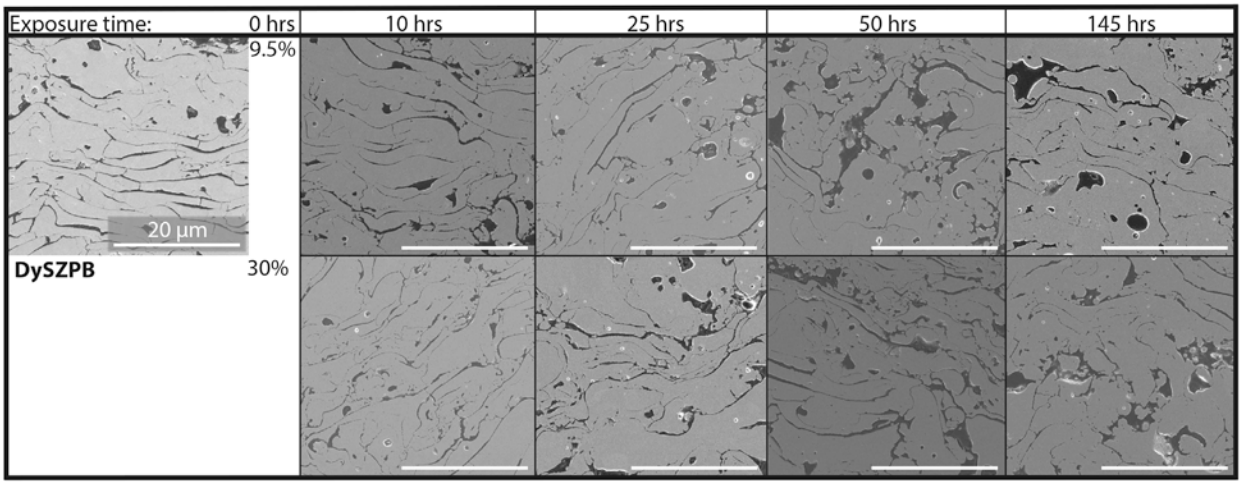

Figure 21: SEM images showing the progression of the microstructures of the DySZPB coatings with aging.

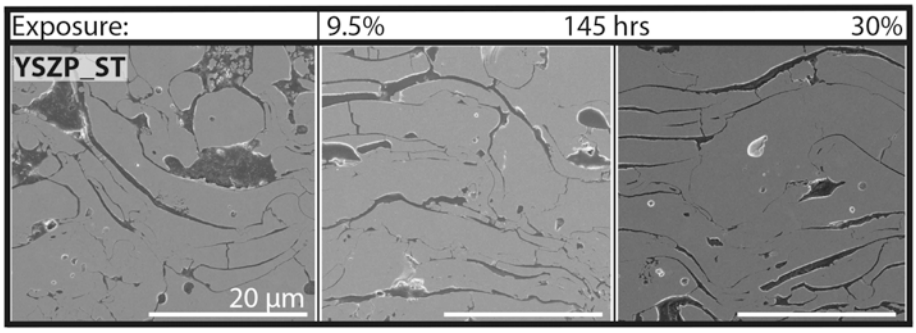

Figure 22: SEM images showing the progression of the microstructures of the YSZP_ST coatings with aging at 145 hours.

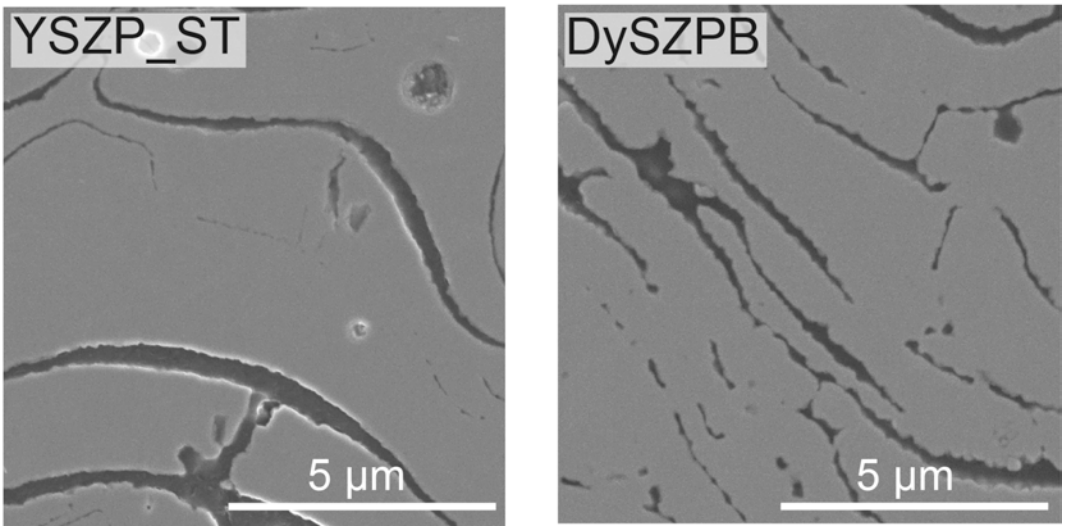

Figure 23: SEM of YSZP and DySZPB coatings exposed at 9.5% water vapor for 145 hrs. showing the further extent of sintering seen in the DySZPB coatings at higher magnification.

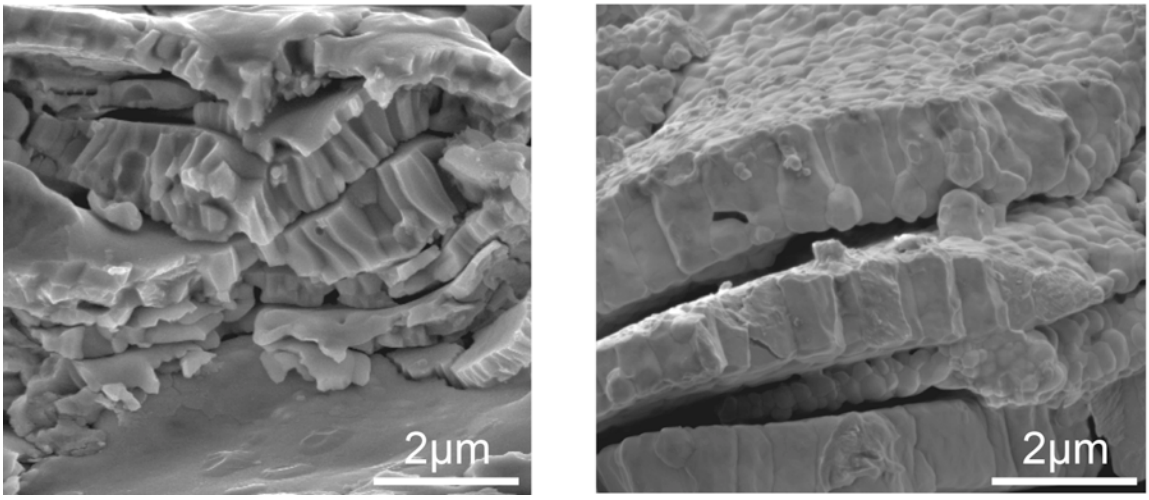

Figure 24: Fracture surface SEM images of as processed and aged DySZPB (70 hrs. shown).

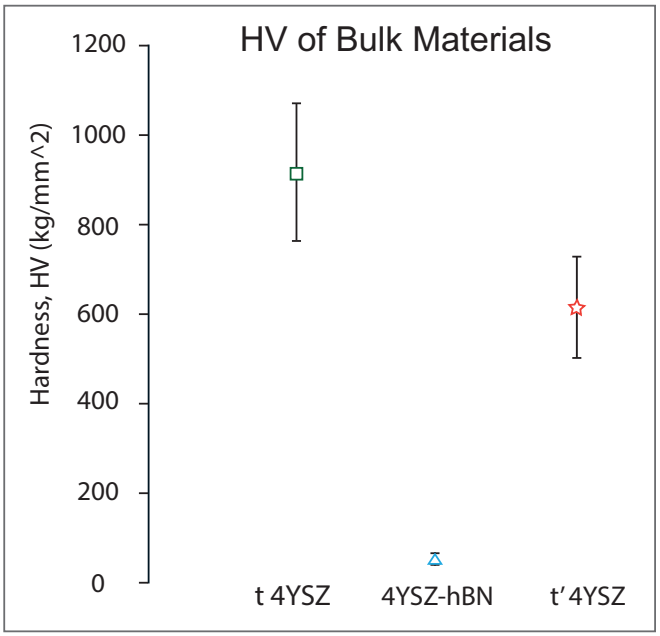

Figure 25: Vicker's hardness compared for the bulk t YSZ, t' YSZ, and YSZ-hBN composite.

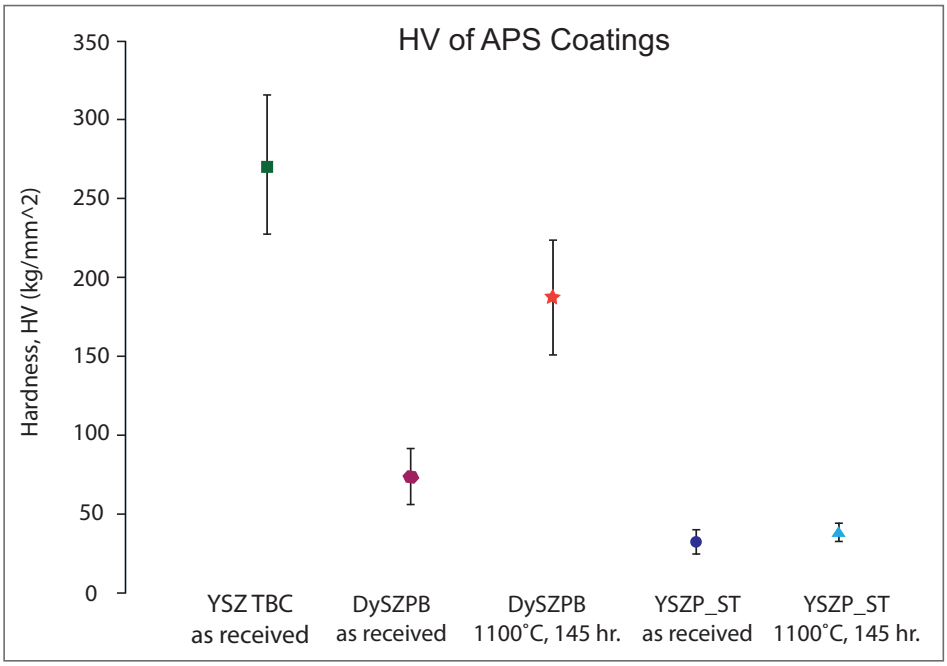

Figure 26: Vicker's hardness of as processed and aged coatings as compared to a standard 4YSZ APS TBC.

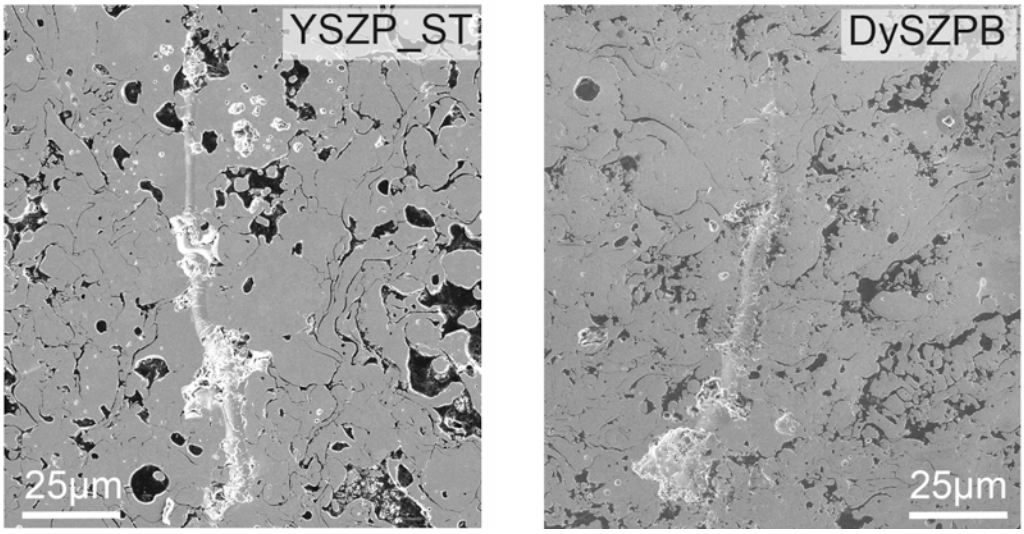

Figure 27: SEM images of the as received APS coatings scratched with the nanoindenter.

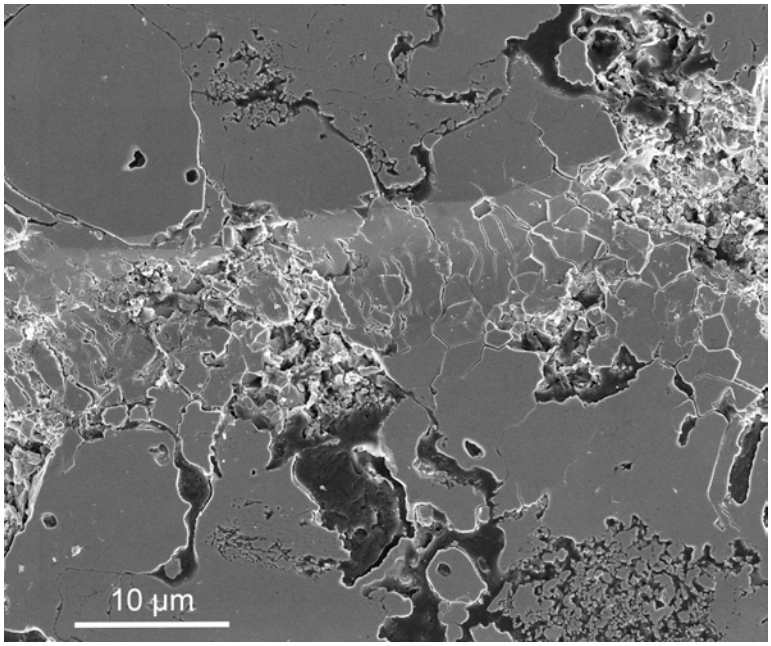

Figure 28: SEM image of the nanoindenter scratch track of the as processed YSZP_ST1q showing surface and radial cracking.

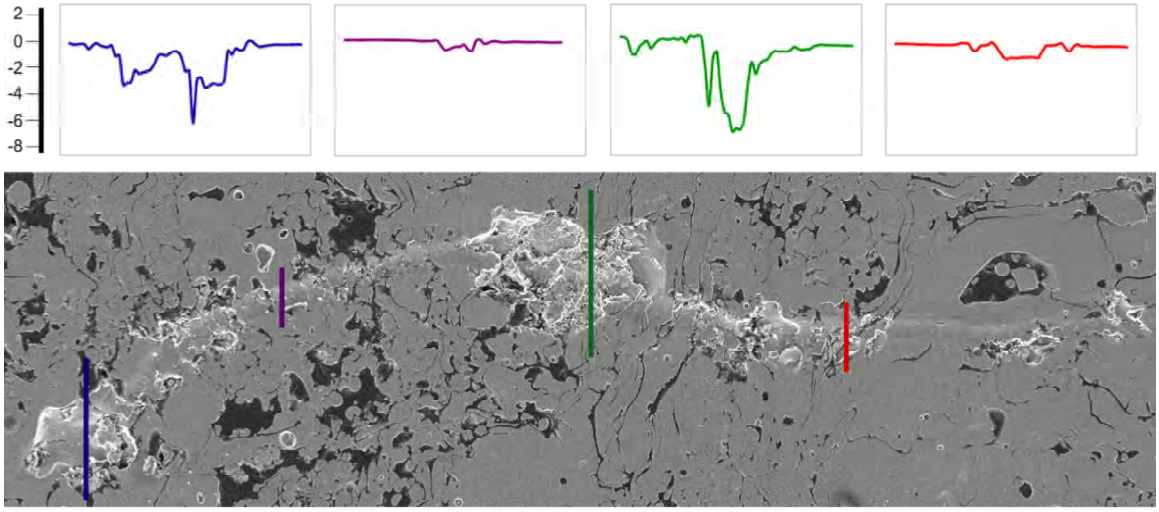

Figure 29: SEM image and measurements of the scratch track by optical vibrometer showing the as processed nanoindenter scratched DySZPB coating.

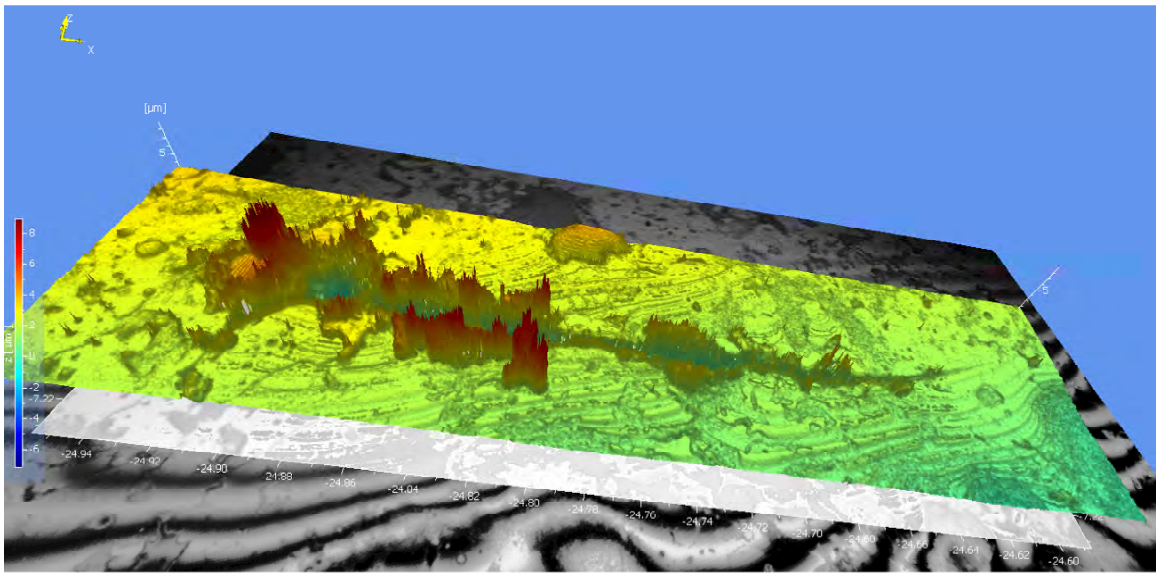

Figure 30: 3D optical vibrometer image of the YSZP_ST coating aged for 145 hrs at 30% H_2O (v) showing material pileup along the edges of the scratch track made by progressive loading with the nanoindenter tip.

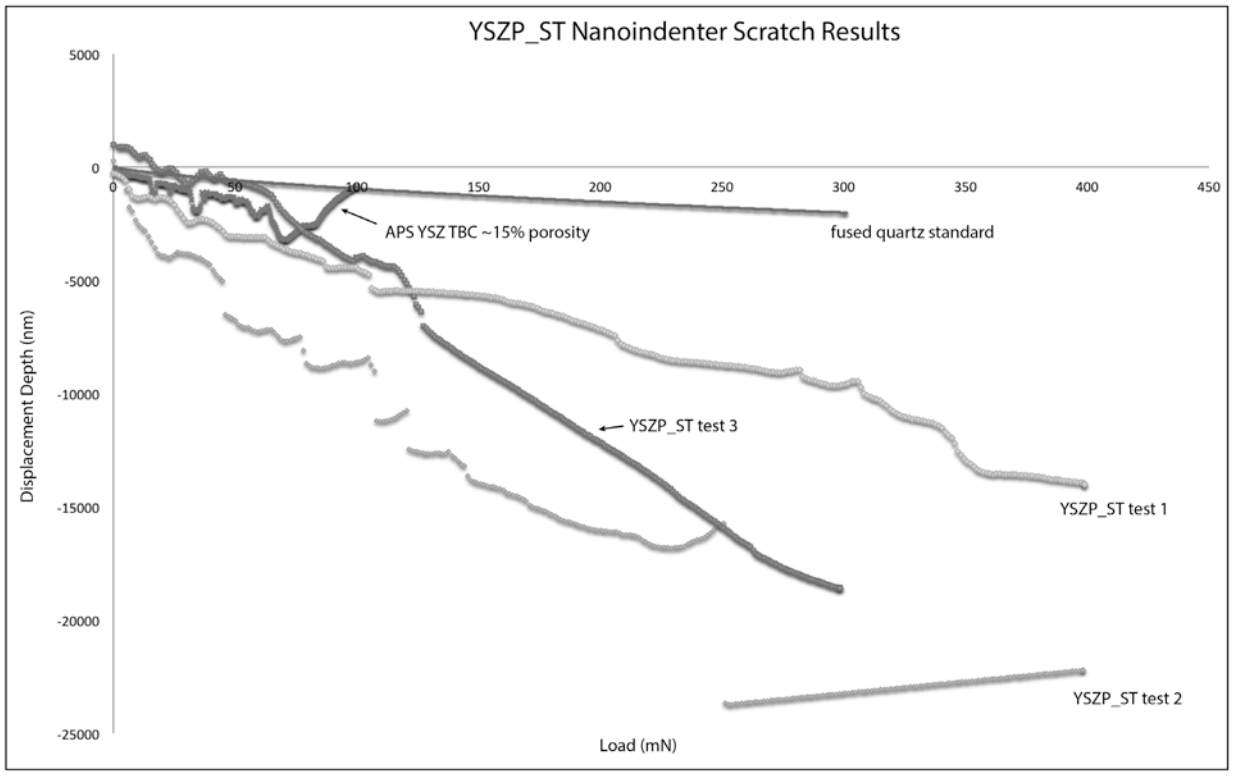

Figure 31: Raw data from the nanoindenter scratch test showing inconsistent measurements of the APS coatings.

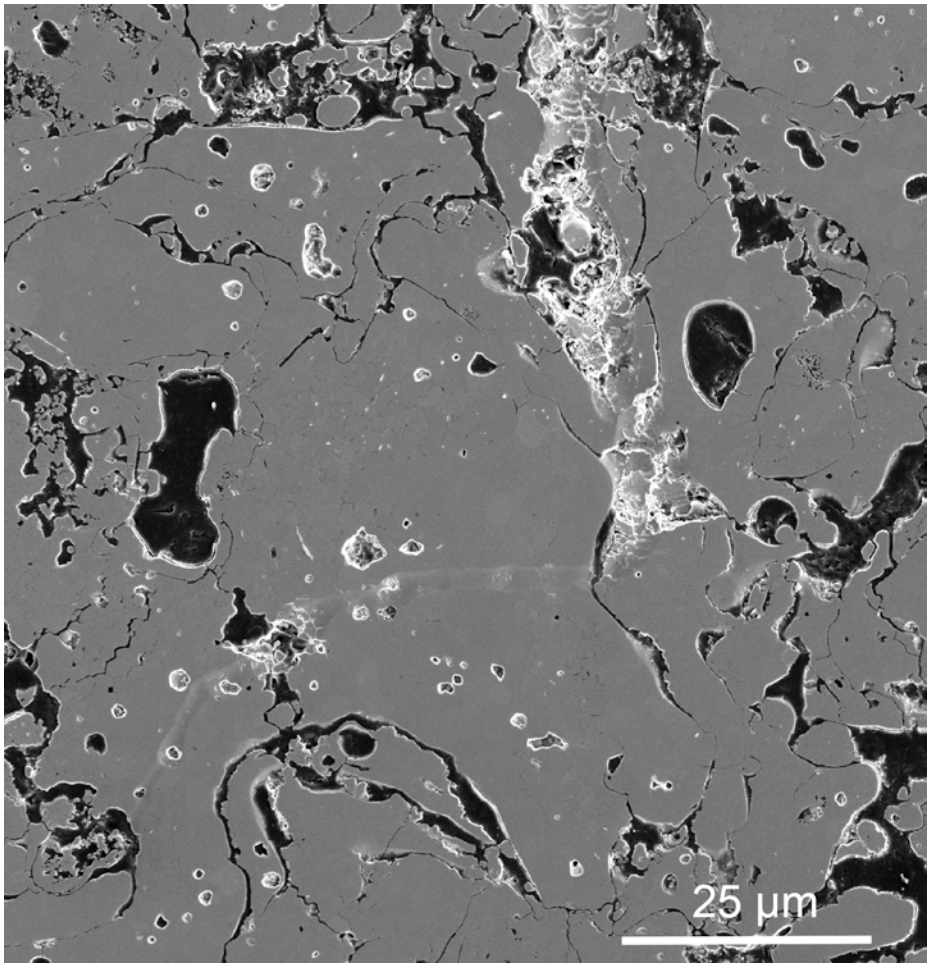

Figure 32: SEM image of the as processed YSZP_ST coating showing a high tortuous scratch track.

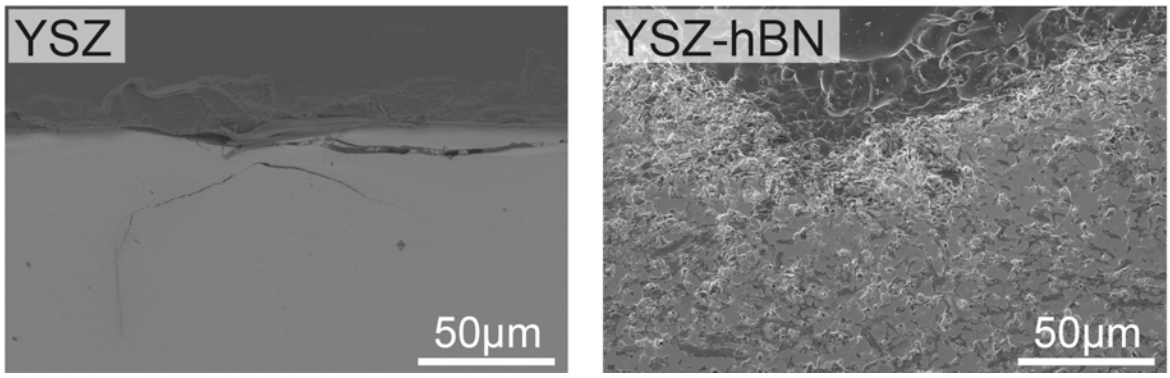

Figure 33: Cross sectional SEM images showing the damage zones of the bulk materials post macroscratch testing.

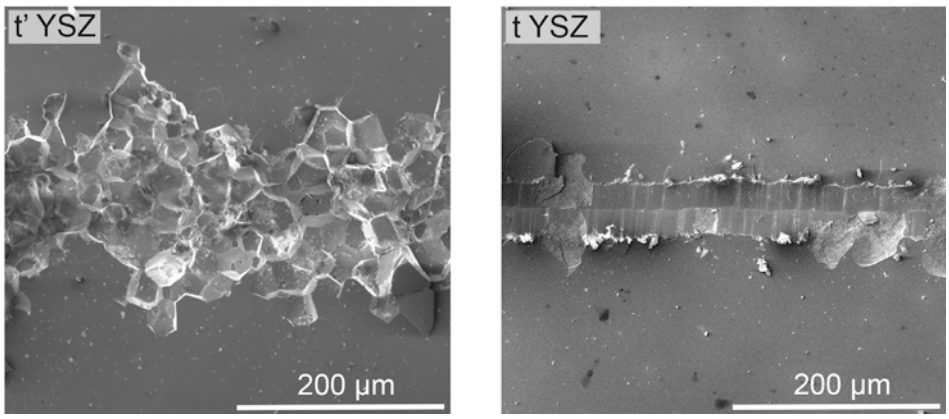

Figure 34: SEM image of the t and t' YSZ macroscratch tracks showing the highly transgranular fracture seen in the SPS processed t' YSZ.

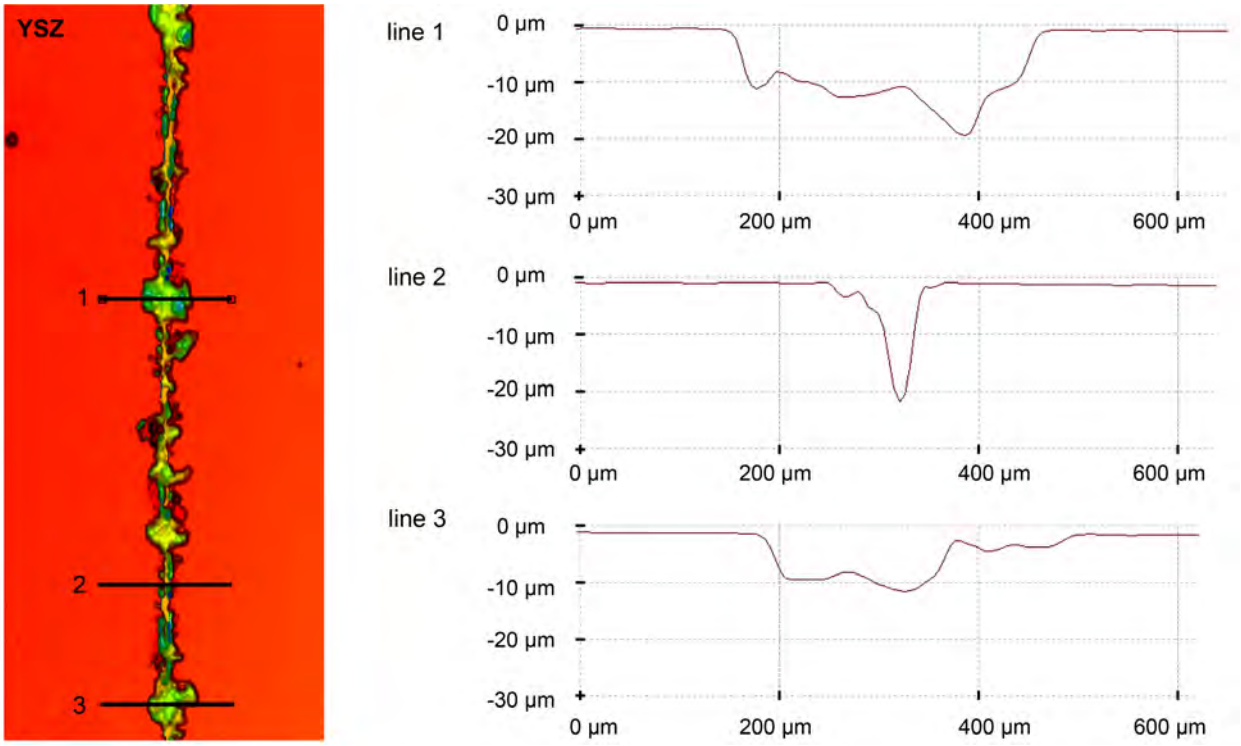

Figure 35: Optical vibrometer topography image and line scans for macroscratched bulk YSZ, taken with vibrometer preset surface parameter ‘smooth with step’.

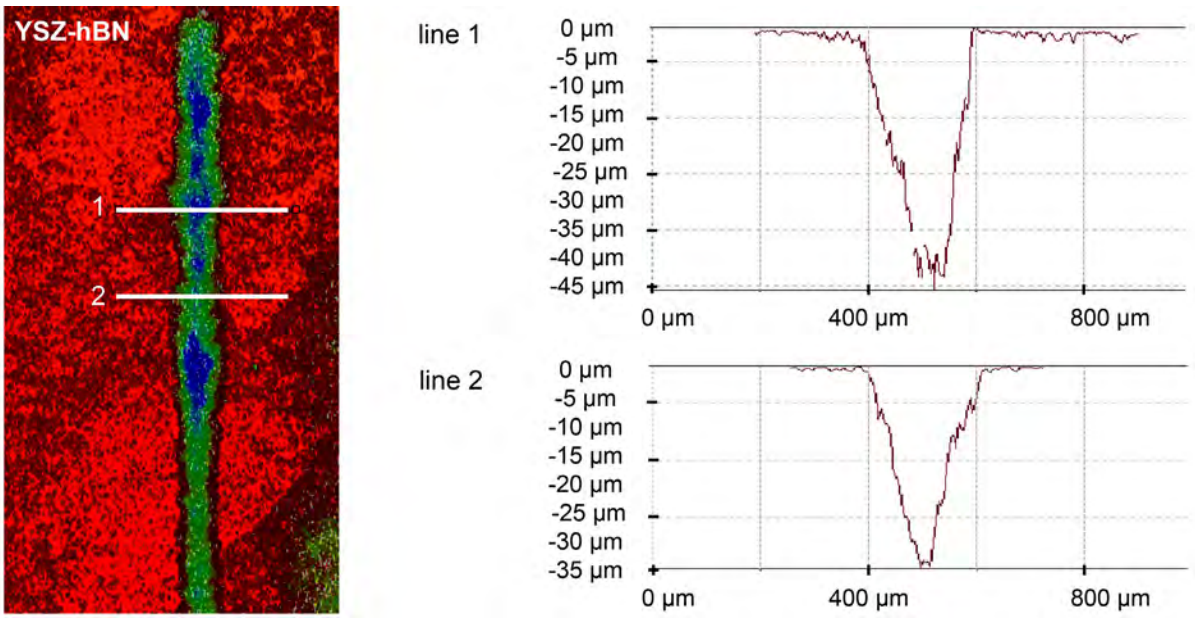

Figure 36: Optical vibrometer topography image and line scans for macroscratched bulk YSZ-hBN, taken with vibrometer preset surface parameter ‘rough’ due to the rougher surface in the composite from pullout during polishing.

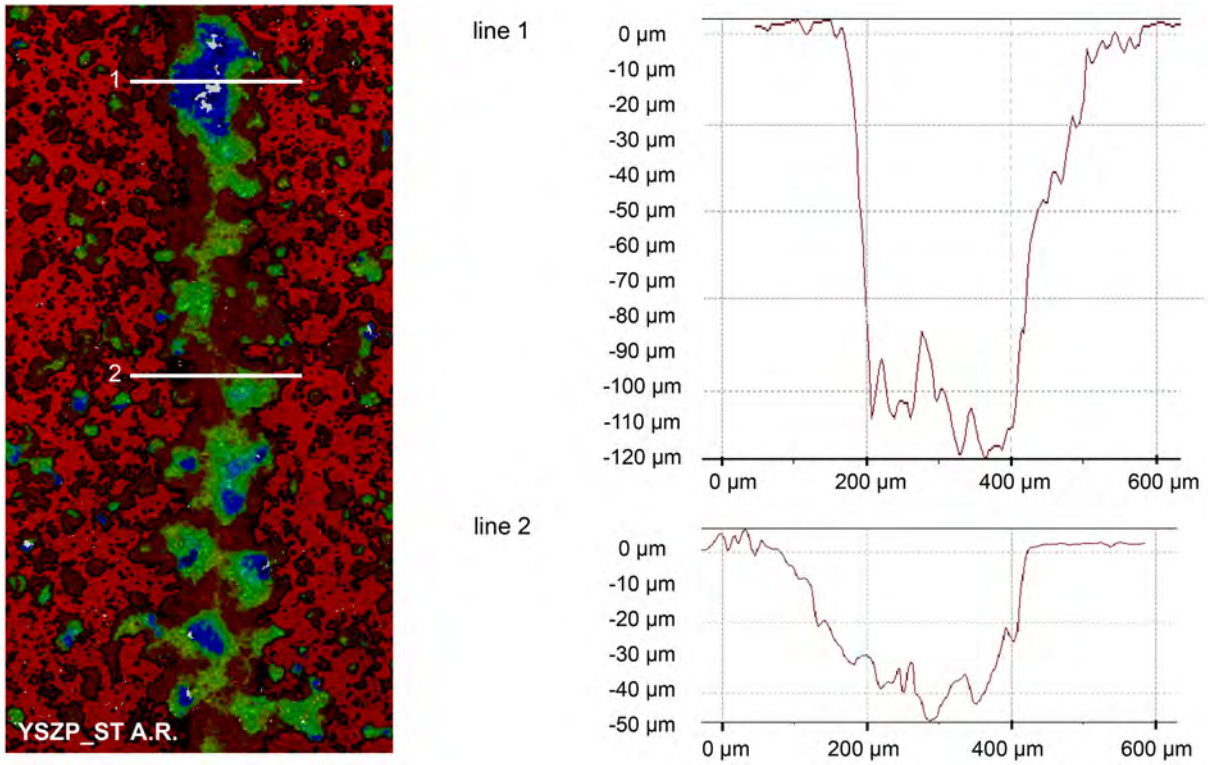

Figure 37: Optical vibrometer topography image and line scans for macroscratched YSZP.

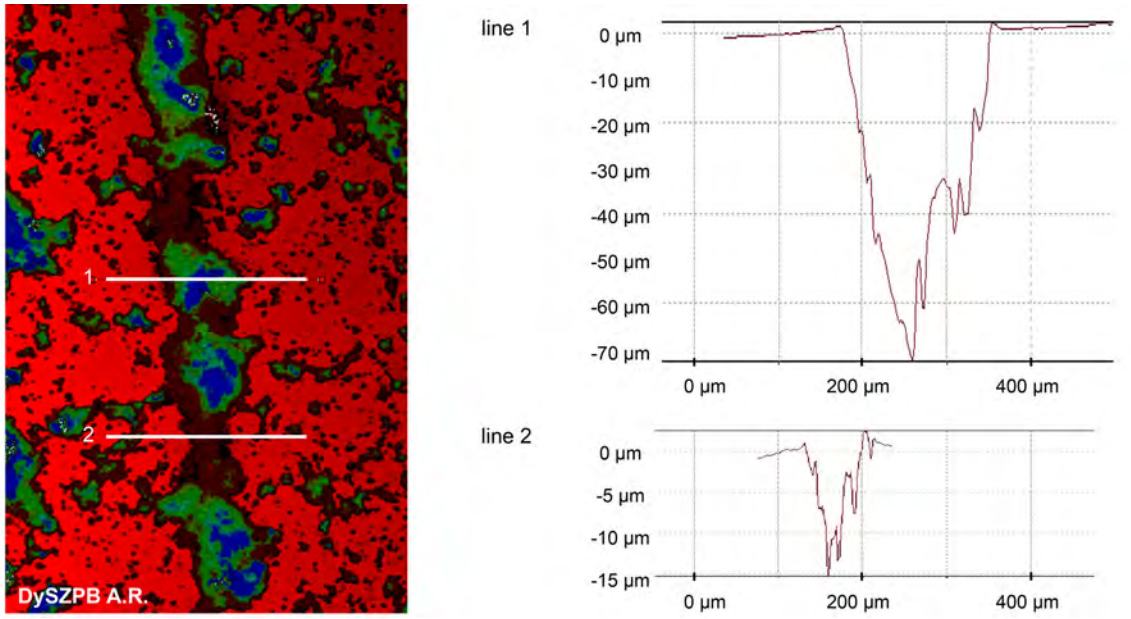

Figure 38: Optical vibrometer topography image and line scans for macroscratched DySZPB.

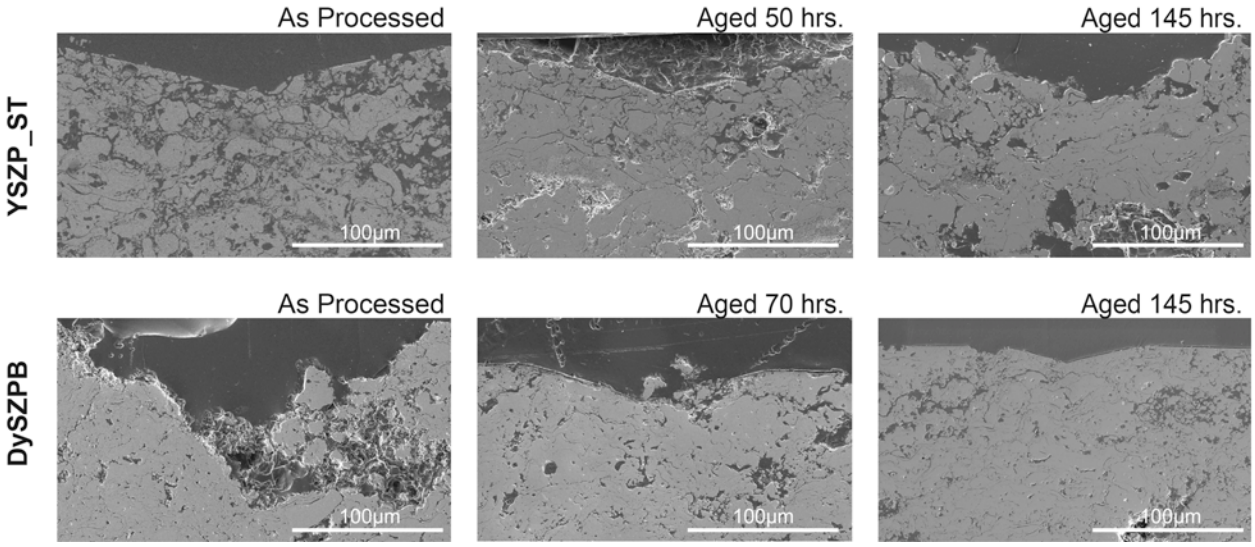

Figure 39: Cross sectional SEM images showing the damage zone evolution for macroscratched YSZP_ST and DySZPB coatings with aging.

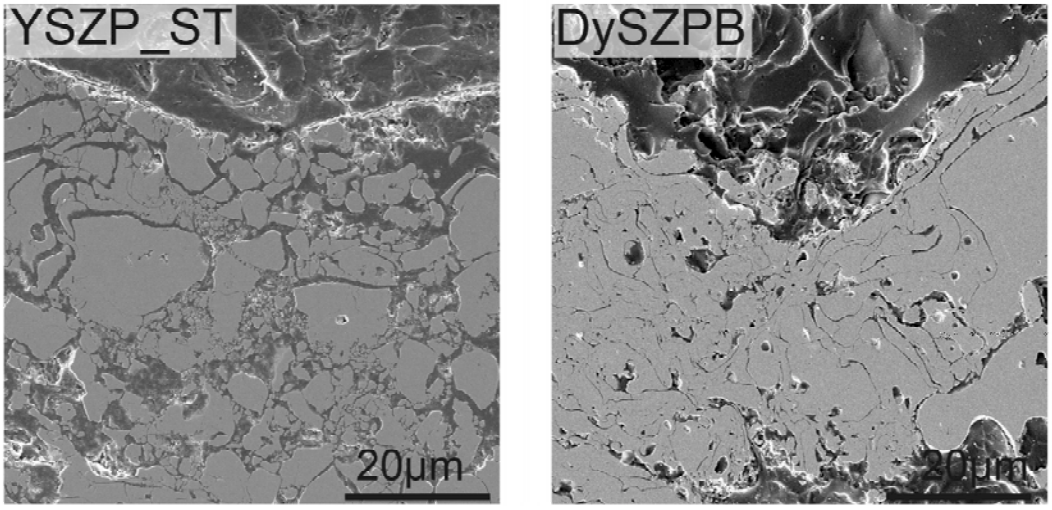

Figure 40: Higher magnification cross sectional SEM images showing the different damage zone characteristics in the YSZP_ST (aged, 50 hrs. shown for example) versus DySZPB (as processed shown).

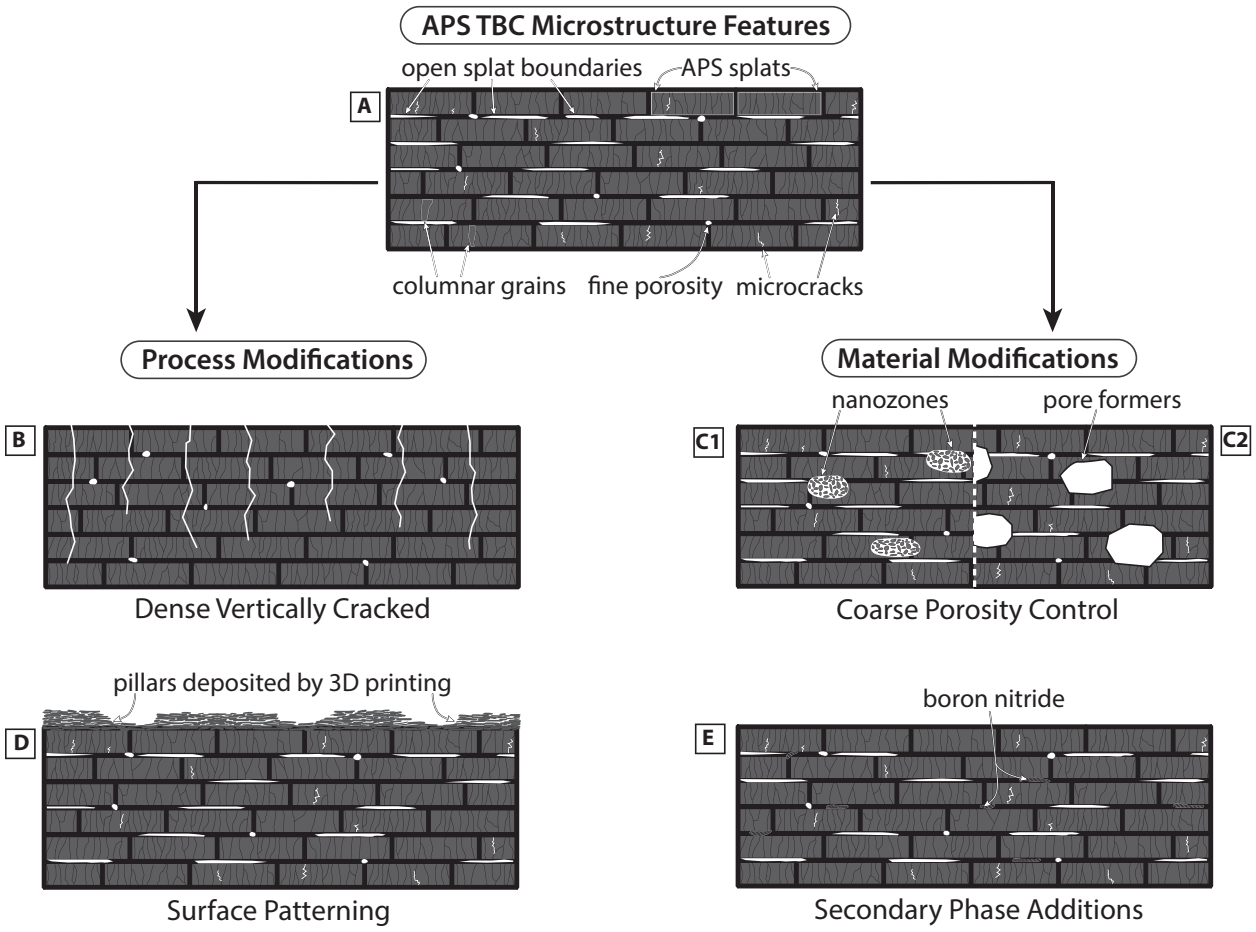

Figure 41: Schematic showing different design strategies for enabling abradability in ceramic APS coatings. Image A shows typical APS microstructural features, while images B and D show process modifications, such as dense vertical cracked microstructures (B) or pillars deposited on the coating surface (D). Images C1, C2, and E show material modifications. C1 and C2 show nanozone features and coarse porosity while E shows secondary phase additions.